Clim Dyn (2018) 51:283–304
DOI 10.1007/s00382-017-3920-6

The application of nonlinear local Lyapunov vectors to the Zebiak–Cane model and their performance in ensemble prediction

Zhaolu Hou[1,2] · Jianping Li[3,4] · Ruiqiang Ding[1,5] · Jie Feng[6] · Wansuo Duan[1]

Received: 10 May 2017 / Accepted: 14 September 2017 / Published online: 25 September 2017

Abstract Nonlinear local Lyapunov vectors (NLLVs) are the nonlinear extension of the Lyapunov vectors (LVs) based on linear error growth theory. As a development of bred vectors (BVs), NLLVs retain the time-saving, simply-applied and flow-dependent advantages of BVs. However, unlike BVs, NLLVs correspond not only to the leading LV but also to other orthogonal LVs. In this paper, NLLVs are applied to the Zebiak–Cane (ZC) coupled model. First, using the analysis data from the ensemble Kalman filter, we explore the effect of the parameters of the breeding process on calculating the NLLVs. It is found that the statistical properties of NLLVs are not very sensitive to the breeding parameters. However, the higher NLLVs (i.e., excluding NLLV1) show temporal randomness. Then, we study the characteristics of the spatial structures and growth rates of different NLLVs. The different NLLVs each have a certain probability of being the fastest error growth direction and together construct the error growth subspace of the ZC model. Compared with BVs, the NLLVs have some advantages in terms of the relationship between the generated error growth subspace and the analysis errors. The NLLVs also have higher local dimensionality than the BVs. NLLVs, as initial ensemble perturbations, are applied to the ensemble prediction of ENSO in a perfect environment. Compared with the results obtained using ensembles employing the random perturbation technique and the BV method, the present results demonstrate the advantages of using the NLLV method in ensemble forecasts.

✉ Jianping Li
ljp@bnu.edu.cn

✉ Ruiqiang Ding
drq@mail.iap.ac.cn

1 State Key Laboratory of Numerical Modeling for Atmospheric Sciences and Geophysical Fluid Dynamics, Institute of Atmospheric Physics, Chinese Academy of Sciences, Beijing 10029, China

2 College of Earth Science, University of Chinese Academy of Sciences, Beijing 10049, China

3 State Key Laboratory of Earth Surface Processes and Resource Ecology and College of Global Change and Earth System Science, Beijing Normal University, Beijing 100875, China

4 Laboratory for Regional Oceanography and Numerical Modeling, Qingdao National Laboratory for Marine Science and Technology, Qingdao 266237, China

5 College of Atmospheric Sciences, Plateau Atmosphere and Environment Key Laboratory of Sichuan Province, Chengdu University of Information Technology, Chengdu 610225, China

6 Global Systems Division, Earth System Research Laboratory/Oceanic and Atmospheric Research/National Oceanic and Atmospheric Administration, Boulder, CO, USA

1 Introduction

Climate prediction on the seasonal scale by dynamical models has been an important topic in geosciences over the last decade (e.g., Hastenrath 1995; Chen et al. 2004; Randall et al. 2007; Smith et al. 2007; Meehl et al. 2014; Saha et al. 2014). The sea surface temperature (SST) provides the lower boundary conditions for the atmosphere and the prediction signal for climate prediction with a lead time longer than 2 weeks (Shukla et al. 2000). Therefore, it is necessary to estimate the future state of the SST field, particularly that in the tropical Pacific Ocean. Most interannual SST variability over the tropical Pacific can be explained by the El Niño–Southern oscillation (ENSO). ENSO also exerts a strong influence beyond the tropical Pacific

through atmospheric teleconnection that affect patterns of weather and climate variability worldwide (McPhaden et al. 2006). For example, the Asian summer monsoon is weaker and its outbreak delayed in El Niño (the warm phase of ENSO) years (Ju and Slingo 1995). Therefore, it is important to predict the onset and development of ENSO. As one of the most predictable climate fluctuations on the planet, ENSO is currently predicted dynamically by many climate models (Wittenberg et al. 2006; Kirtman and Min 2009; Zheng et al. 2009; Saha 2014; Barnston et al. 2015). Currently, there are 17 dynamical models employed in the International Research Institute ENSO forecast (http://iri.columbia.edu/our-expertise/climate/forecasts/enso/current/?enso_tab=enso-cpc_update).

The dynamical models of ENSO are multidimensional complex systems and their outputs are sensitive to the initial inputs. Therefore, the output results of ENSO models, including many oceanic and atmospheric variables, are influenced by the uncertainty in oceanic and atmospheric initial conditions (Moore and Kleeman 1998). To describe and reduce the degree of uncertainty associated with the initial situations, one can obtain many parallel but different prediction results using an ensemble. Ensemble prediction can provide probabilistic forecasts of the future state of the system through certain sampling approaches (Leith 1974; Kalnay 2003). If a group of initial states samples the uncertainty of the initial analysis states (input data) reasonably well, we can integrate these different initial states into the various predictand states. Then, the average of the group of predictand states performs better than the single predictand and the spread of the group can provide the second moment of the ensemble, which are generally used as the quantification of the uncertainty of the result (Houtekamer and Derome 1995; Buizza and Palmer 1998; Moore and Kleeman 1998; Palmer et al. 1998; Houtekamer and Zhang 2016). To perform ensemble prediction, we need to generate different initial ensemble members. The basic principle of the generation of initial ensemble members is to sample the initial error probability spaces of the initial analyses (Epstein 1969; Leith 1974; Toth and Kalnay 1997). Based on dynamical error growth theory, various ensemble generation schemes have been introduced and applied to ENSO prediction and predictability. These include the bred vector (BV) method (Toth and Kalnay 1993, 1997; Cai et al. 2003; Yang et al. 2006, 2009), the singular vector (SV) method (Lorenz 1965; Molteni et al. 1996; Cheng et al. 2010a, b), the conditional nonlinear optimal perturbation (CNOP) method (Mu et al. 2007; Duan et al. 2009; Duan and Mu 2009), and stochastic optimal theory (Tang et al. 2005). Recently, some promising methods based on the Kalman filter concept have been proposed and applied to ensemble forecasting, such as the ensemble transform rescaling developed from the BV scheme (Wang and Bishop 2003) and the ensemble Kalman filter (EnKF) (Bishop and Toth 1999; Wei et al. 2006; Zheng et al. 2006; Wu 2016). But their application to ENSO predictions is still in the course of development.

Compared with other ensemble generation schemes, the BV method is a time-efficient approach (Wang and Bishop 2003). The BV is an extension of the leading Lyapunov vector (LV) to a nonlinear model, with finite-time evolution and finite-size perturbation (Toth and Kalnay 1993, 1997). The leading LV defines the fastest sustainable growing direction in phase space that any infinitesimal perturbation will gradually evolve toward after sufficient integration time (Ginelli et al. 2007), while the BV represents the fastest growing direction of the dynamical system in the nonlinear context. The BVs can be acquired by the breeding process. The breeding process contains periodic rescaling to keep the perturbation within a given amplitude range, which is similar to the data assimilation cycle; the BVs are rescaled to a given amplitude by the analysis or reference trajectory instead of by observations. This similarity ensures that the BV can capture the main spatial structure of the forecast errors and the growing part of the analysis errors. The breeding process can be applied at every initial state and acquires the flow-dependent unstable directions as BVs. The flow-dependent BVs have been applied to different ENSO dynamical systems (Cai et al. 2003; Yang et al. 2006, 2008, 2009, 2010; Tang and Deng 2011; Baehr and Piontek 2014). The structures of the BVs are closely associated with the real-time forecast error and evolve with the background ENSO phase, and the growth rates of BVs are a function of the season and ENSO phases (Yang et al. 2006, 2008). Meanwhile, BVs used as ensemble perturbations can improve the prediction skill of the ENSO prediction and be used to construct the background error covariance matrix in tropical ocean data assimilation (Yang et al. 2009).

However, BVs have certain limitations because in theory they are only a nonlinear extension of the leading LV. Previous studies found that although various BVs are generated from different initial random perturbations or through different normalizations in the operational environment, they tend to have increasing projections onto the most unstable growing direction (i.e. the leading LV) through successive evolution driven by the same underlying background dynamical flow (Wang and Bishop 2003; Bowler 2006). The similarity between the structures of BVs may result in an underestimate of ensemble spread. This could be more severe over those local regions with strong instabilities because BVs may be more similar there (Patil et al. 2001). Meanwhile, the complex dynamical models are usually high-dimensional and have multiple independent growth directions, which together collude in error growth. The small subspace of the fastest growing perturbations sampled by the BVs may not always capture the error growth space effectively.

In order to overcome the deficiencies of the BVs, the nonlinear local Lyapunov vectors (NLLVs) have been proposed and developed (Li and Wang 2008; Feng et al. 2014, 2016). NLLVs are the theoretical nonlinear extension of LVs. NLLVs can represent the different directions of the error growth space of the dynamical system from the fastest to slowest. The corresponding growth rates are known as the nonlinear local Lyapunov exponent spectrum (NLLEs) (Chen et al. 2006; Ding and Li 2007). Different NLLVs correspond to different growth rates and different physical processes. There are some differences between NLLVs and BVs. Theoretically, BVs are an extension of the leading LV, while NLLVs are inherited from the leading LV and other orthogonal LVs in a nonlinear framework. Similar to the BVs, in practice NLLVs are also calculated through the breeding process using nonlinear models which maintains the advantages of BVs, i.e. the trivial computational cost and the ease of implementation. However, to avoid different perturbations converging to the fastest error growth direction, the breeding process of NLLVs is coupled with orthogonalization. Therefore, NLLVs that have mutually orthogonal directions can fundamentally describe more broadly the extent of the error growth space than BVs. The NLLVs have been applied to some simple dynamical systems, including the lorenz63 and lorenz96 systems and the barotropic model (Feng et al. 2014, 2016). Feng et al. (2016) found that the NLLVs can indeed capture more directions of analysis errors than the same number of BVs thus having better performance in ensemble prediction.

There are differences between NLLVs and SVs. Following the definition from Legras and Vautard (1996), SVs are the extension of the forward Lyapunov vectors from $t_1 = t_{\text{present}}$ to $t_2 = t_1 + \mathrm{T}$ ($t_1 = t_{\text{present}}$) at initial time, whereas NLLVs as the bred-growing modes (BGMs) have similarities to the backward Lyapunov vectors (Legras and Vautard 1996; Szunyogh et al. 1997) at final time. However, the NLLVs and BVs are calculated using a nonlinear model from $t_1 = t_2 - \mathrm{T}$ to $t_2 = t_{\text{present}}$. NLLVs and SVs both are sets of mutually orthogonal vectors, but BVs not. Obtaining additional SVs requires running the tangent linear model and its adjoint about three times the number of singular vectors required (Molteni et al. 1996). However, NLLVs are directly acquired from the nonlinear model by the breeding process. Without the tangent and adjoint model, the calculation of NLLVs are more time-saving and convenient than SVs. Due to the different origin, we do not lay stress on the linkages between NLLVs and SVs in this paper.

Considering the differences between NLLVs and BVs, we want to explore whether the spatial structures and growth rates of different NLLVs are still related to background flow and ENSO development, and if NLLVs are more effective at describing the error growth subspace than BVs. As the first successful model to simulate and predict ENSO, the Zebiak–Cane (ZC) model is under continual development (Zebiak and Cane 1987; Chen et al. 1999, 2004). This intermediate coupled model does not contain the weather variations, which contribute to the linkages between the error growth and the ENSO process. Therefore, the ZC model is chosen in this paper. The present paper will attempt to apply the NLLVs in the ENSO coupled model and inspect the sensitivity of NLLVs to the parameters of the breeding process. We will focus on the growth rate and spatial structure of different NLLVs and how the performance of the NLLVs as ensemble perturbations compares with the other traditional schemes in the ZC model.

The paper is organized as follows. Section 2 explains the computation process of the NLLVs and introduces the ZC model. Section 3 is devoted to the calculation of NLLVs in the ZC model and the sensitivity of NLLVs to the choice of breeding parameters. The improved performance of NLLVs over BVs will also be shown in this section. Section 4 will demonstrate the relationship between different NLLVs and ENSO in terms of the growth rate and spatial structure. Section 5 describes the benefits of NLLVs as ensemble perturbations. The main conclusions are presented in Sect. 6.

2 Method and model

2.1 Nonlinear local Lyapunov vector

The Lyapunov exponent (LE) and LV are used to study the stability of a dynamical system. However, the LV and LE are based on linear error growth theory. To avoid this limitation, the NLLVs and the corresponding NLLEs based on nonlinear error growth dynamics theory are introduced and developed to describe the nonlinear error growth characteristics (Chen et al. 2006; Ding and Li 2007; Li and Wang 2008; Feng et al. 2014). The NLLVs and NLLEs are the extension of LVs and LEs to the nonlinear context. Their derivation is described in Appendix A.

In line with LVs in the tangent linear system, the NLLVs represent vectors along the directions from the fastest-growing direction to the fastest-shrinking direction of the nonlinear system (Feng et al. 2014). The NLLVs focus on the 'nonlinear and local' characteristics of the system and are functions of the phase space states $\boldsymbol{x}_0$, the initial perturbation vector $\boldsymbol{\delta}$ (both the amplitude and the direction) and a given evolution time Δt.

The NLLVs are calculated through the breeding process (as shown in Fig. 1). Consider a series of successive reference states $\boldsymbol{x}_{-K\cdot\Delta t}, \boldsymbol{x}_{-(K-1)\cdot\Delta t}, \ldots, \boldsymbol{x}_0$ (black line), where Δt is the length of a breeding cycle and K is the cycle number. Add a small random perturbation $\boldsymbol{\delta}_{1,-K\cdot\Delta t}$ of size M (in a certain norm) to $\boldsymbol{x}_{-K\cdot\Delta t}$ and then integrate the perturbed state $\boldsymbol{x}'_{1,-K\cdot\Delta t}$ with the full nonlinear model over an interval Δt to

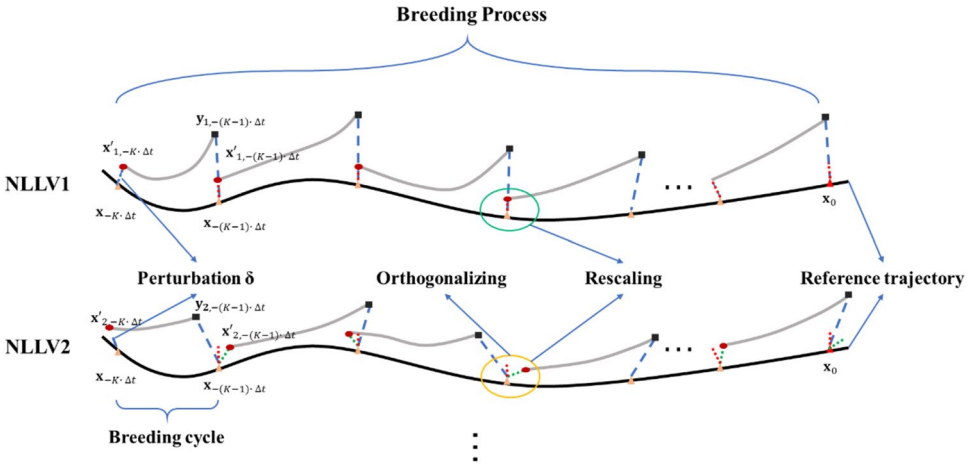

Fig. 1 Breeding process of NLLVs. A breeding process is composed of multiple breeding cycles. A random perturbation is initially added to the reference trajectory at the beginning of the breeding process, and integrated. At the end of each breeding cycle, the NLLVs are orthogonalized by the GSR method and the perturbations are rescaled. The evolved perturbations (blue dashed line) are orthogonalized with the NLLV1 (red dashed line) to give the NLLV2 (green dashed line). Other fastest growing NLLVn are orthogonalized with respect to NLLV1, NLLV2,…, NLLVn–1 (adapted from Feng et al. 2014, 2016)

give $\boldsymbol{y}_{1,-(K-1)\cdot\Delta t}$. Let $\boldsymbol{\delta}'_{1,-(K-1)\cdot\Delta t}$ denote the difference between the $\boldsymbol{y}_{1,-(K-1)\cdot\Delta t}$ and the corresponding reference $\boldsymbol{x}_{-(K-1)\cdot\Delta t}$. $\boldsymbol{\delta}'_{1,-(K-1)\cdot\Delta t}$ is then rescaled to the size of the initial perturbation M, to give the updated perturbation $\boldsymbol{\delta}_{1,-(K-1)\cdot\Delta t}$. Then superpose the rescaled perturbation $\boldsymbol{\delta}_{1,-(K-1)\cdot\Delta t}$ onto the subsequent reference state $\boldsymbol{x}_{-(K-1)\cdot\Delta t}$, integrate and scale for K cycles to $\boldsymbol{x}_0$ to derive NLLV1 or BV.

To calculate the NLLV2, superpose another different perturbation $\boldsymbol{\delta}_{2,-K\cdot\Delta t}$ of size M on the same reference states and integrate for a breeding cycle to acquire the forecast states $\boldsymbol{y}_{2,-(K-1)\cdot\Delta t}$. The differences between the perturbed forecast and the reference states are denoted by $\boldsymbol{\delta}'_{2,-(K-1)\cdot\Delta t}$. At the end of every breeding cycle, orthogonalize $\boldsymbol{\delta}'_{2,-(K-1)\cdot\Delta t}$ with respect to the first perturbation $\boldsymbol{\delta}_{1,-(K-1)\cdot\Delta t}$ using the Gram–Schmidt orthonormalization (GSR) algorithm (Li and Wang 2008; Wolf et al. 1985) and scale to size M, to give $\boldsymbol{\delta}_{2,-(K-1)\cdot\Delta t}$. As shown in Fig. 1, integrate, orthogonalize with the corresponding $\boldsymbol{\delta}_{1,-i\cdot\Delta t}$ and scale the perturbation $\boldsymbol{\delta}_{2,-i\cdot\Delta t}$ through K breeding cycles to $\boldsymbol{x}_0$ to obtain the NLLV2. The process of calculating the subsequent NLLVn is similar to that of the NLLV2, but in every breeding cycle the perturbation is orthogonalized with all the $\boldsymbol{\delta}_{n,-i\cdot\Delta t}$ from NLLV1 to NLLVn–1 using the GSR algorithm. Then, NLLVs corresponding to the $\boldsymbol{x}_0$ are acquired.

Multiple BVs can be obtained by simply selecting different initial random seeds. Through the dynamical evolution, the random components in the initial perturbations will be gradually eliminated. Therefore, the BVs have dominant projections on the leading LV and span the small space of the fastest growing directions. However, unlike the BVs, the NLLVs undergo orthogonalization in every breeding cycle. This operation ensures that the differently directed perturbations develop fully. The NLLVs have a more stable performance in sampling the error growth subspace.

The breeding parameters of the breeding process, such as the initial perturbation size M and scale temporal interval Δt, determine the scale of the spatial and temporal instability represented by the NLLVs. Thus, these parameters are chosen to be appropriate for the problem to be studied. In Sect. 3, we will calculate the NLLVs in the ZC model and check the sensitivity of the NLLVs and the growth rates (NLLEs) to the breeding parameters.

2.2 Zebiak–Cane model

In this study, we use the standard version of the ZC model, a nonlinear model of intermediate complexity. The ZC model is an anomaly coupled model that describes anomalies about a specified seasonally varying climatological state. It has been widely used in prediction and predictability studies over several decades (Zebiak and Cane 1987; Blumenthal 1991; Chen et al. 2004; Mu et al. 2007; Cheng et al. 2010a, b; Duan et al. 2014).

The model is composed of a Gill-type steady-state linear atmospheric model and a reduced-gravity oceanic model (Zebiak and Cane 1987). The oceanic dynamics is described by a linear reduced-gravity model with a rectangular ocean basin that extends from 124°E to 80°W and from 29°N to 29°S on a 2° longitude × 0.5° latitude grid. The atmospheric dynamics follows the steady-state linear shallow water equations on an equatorial beta-plane. The circulation is forced by a heating anomaly that depends partly on local heating that is associated with SST anomalies (SSTAs) and on

low-level moisture convergence (parameterized in terms of the surface wind convergence). Considering that the moisture-related heating is operative only when the total wind field is convergent, the convergence feedback is nonlinear. The thermodynamics describe the evolution of temperature anomalies in the model surface layer. The evolution equation of the SSTA in the tropical Pacific includes three-dimensional temperature advection by the specified mean currents and the calculated anomalous currents. The model time step is 10 days.

3 Calculation of NLLVs in the ZC model

The NLLVs and BVs are dependent on the background flow. Different reference trajectories correspond to different NLLVs and BVs. Different breeding parameters determine the physical meaning of the NLLVs produced by the breeding process. Therefore, this section explores how to obtain the reference trajectories and how to choose the breeding parameters sensibly. The important point is to clarify the sensitivity of the NLLVs to these parameters. Vialard et al. (2005) found that the uncertainties in the SST determine the spread of ensemble forecasts, while perturbation of the wind stress or atmospheric internal variability is less efficient. Therefore, we will focus on the SST field of the NLLVs and explore the instabilities in the spatial structure of the SST field.

3.1 Configuration of the reference trajectory

For greater consistency with the operational application, the reference states (analysis data) are constructed using the EnKF assimilation method (Evensen 2003). A detailed description of the EnKF method is given in Appendix B. Cai et al. (2003) directly calculated BV using the true trajectory and simply used random perturbations as analysis errors to compare BV and random perturbation methods in the ensemble experiment. This approach is unreasonable because the random errors contain less fast growing pattern than that of analysis errors from the assimilation process (Toth and Kalnay 1997). Here, analysis errors from the EnKF assimilation method—as the difference between the analysis data and the true data—are constrained by dynamical equations, which tallies with the operational environment.

All experiments in the present paper assume a perfect model under which the output of a long-period integration from the model is regarded as the true trajectory. The observations to be assimilated are obtained by adding a random noise to the true trajectory. Here we just assimilate the variable—SSTA (TO in the ZC model)—which is the key variable in the air–sea interaction. We assume that the locations of observations are as in Fig. 2, which shows the observation stations from the tropical atmosphere–ocean (TAO) buoy array. We choose to use only a subset of the TAO observation locations because of the high spatial correlation of the SSTA field in the ZC model. The total number of observation locations is 24. If a vector TO_{tru} denotes the true state and TO_{obs} is the observation field of SSTA, then:

$$TO_{obs} = H \cdot TO_{tru} + \varepsilon, \tag{1}$$

where H is the observation operator that defines the functional relation from the model space to the observational space. The added noise error ε has a Gaussian distribution of $\mathbb{N}(0, 0.6^2)$ for the ZC model, where $\mathbb{N}$ denotes the sample space of the Gaussian distribution, 0 is the expectation and 0.6 is the standard deviation. The value 0.6 °C is approximately the root mean square error (RMSE) of SST observations (Reynolds 1988; May et al. 1998). In the EnKF data assimilation method, we use 200 members and adopt the inflation ratio 5% to the ensemble members to prevent filter divergence. The assimilation interval is 1 month. The assimilation time is from the 132.5th to the 5132.5th month of the model time. The RMSE of the Niño 3 index (150–90°W, 5°S–5°N) is 0.198 °C, which is roughly 15% of the Niño 3 index standard deviation. The RMSE of SSTA in space is 0.178 °C and the spread error of the spatial SSTA is 0.238 °C, which indicates that filter divergence is not present. The RMSE and spread evolve smoothly with time from the 400.5th month, which demonstrates the suitability of the

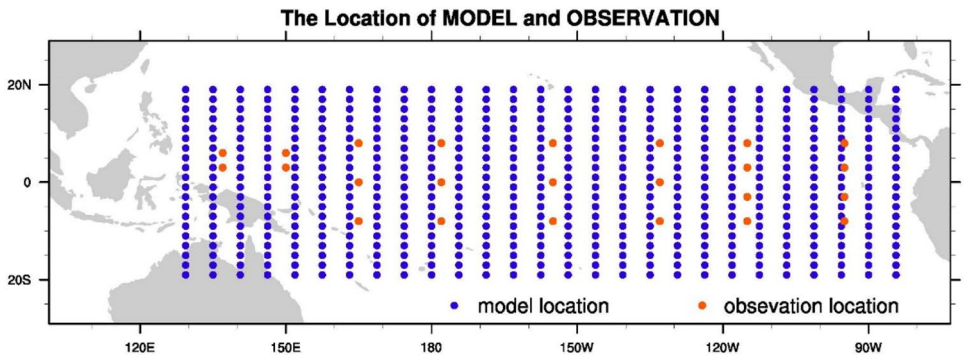

Fig. 2 Distribution of model (blue) and observation (orange) locations. Locations of the observations are a subset of the TAO/TRITON array standard moorings

assimilation parameters and process. The Niño 3 indexes of both the analysis and true trajectory are illustrated in Fig. 3, spanning 250 years. The Niño 3 index shows obvious decadal/interdecadal variations in this period. During this time window, the RMSE of the SSTA (TO), surface zonal wind anomaly (UO), surface meridional wind anomaly (VO) and oceanic upper layer depth averaged onto the coarser grid (H1) are 0.199, 0.253, 0.167, and 5.90, respectively.

3.2 Sensitivity of NLLVs to the breeding parameters

Once the analysis states are generated, the NLLVs can be calculated through the breeding process. As shown in Fig. 1, a breeding process consists of multiple breeding cycles. In every cycle, the perturbations are added to the reference state and grow freely. At the end of each cycle, the developed perturbations are re-orthogonalized using the GSR method and rescaled. Through the breeding process, the different initial random perturbations evolve into the different NLLVs. To make sure that the NLLVs represent the unstable structures of the temporal and spatial scales of interest, we need to choose appropriate parameters for the breeding process: breeding variables, rescaling interval, rescaling factor, and rescaling size.

3.2.1 Reference breeding parameters and snapshots of NLLVs

The breeding variables are the variables to be rescaled and orthogonalized. We should choose these variables such that they contain information on the instabilities of interest at some particular scale. In the ENSO cycle, the SST is a key variable; it reflects the ocean state and directly forces the tropical atmosphere. Changes of SST characterize the different phases of ENSO. Therefore, the SSTA (TO in the model) is chosen as the breeding variable. The thermocline depth (H1 in the model) represents the energy of the upper ocean and directly influences the SST. Meanwhile,

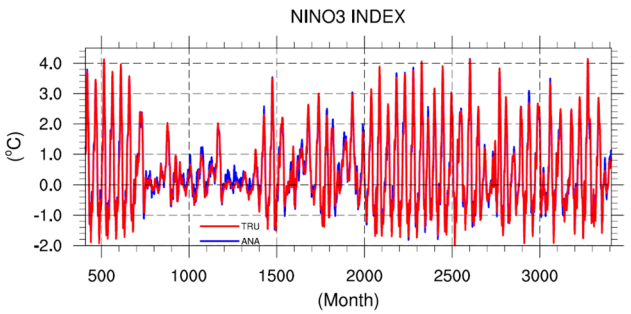

Fig. 3 Niño 3 index for the analysis and true trajectory from the 408.5th to 3407.5th months of model time. The analysis Niño 3 index is consistent with the true index. The Niño 3 index shows obvious decadal/interdecadal variations in this time window

the wind stress from the atmosphere component: the zonal wind anomaly (UO) and surface meridional wind anomaly (VO), drives the ocean circulation and plays an important role in ENSO evolution. Cai et al. (2003) chose these four variables to calculate BV. We also choose these two oceanic variables and two atmospheric variables, SST (TO), H1, UO, and VO, as the breeding variables for the NLLV.

The rescaling interval, the time scale of a breeding cycle, is a little arbitrary. Peña and Kalnay (2004) argued that the interval should be longer than 2 weeks for the slowly varying coupled instability of ENSO. Cai et al. (2003) used 3 months to obtain BV for the ZC model, Yang et al. (2006) used 1 month for a coupled global general circulation model, and Tang and Deng (2011) adopted 1 month in a hybrid coupled model. In this study, we choose a rescaling period of 1 month in the ZC model.

The rescaling factor is based on the Euclidean distance [Eq. (2) of SSTA over the model domain]. SSTA (TO) is chosen here because of its critical importance in ENSO simulation and prediction (Tang and Deng 2011). The SSTA marks the ENSO evolution and may contain some information with which to predict the future ENSO phase. Cai et al. (2003) found that the BV is, in fact, relatively insensitive to the definition of the rescaling norm. We will test this point for NLLVs using different norm definitions from a statistical view below. Here, the rescaling factor γ_{sst} is defined as

$$\gamma_{sst} = \sqrt{\frac{\sum_{i=1}^{N} \left(TO_i^{pre} - TO_i^{ana}\right)^2}{N-1}}, \tag{2}$$

where TO_i^{pre} is the ith spatial grid point of the evolved SSTA field from the perturbed initial state and TO_i^{ana} is the corresponding ith grid of the reference state (i.e., the analysis data) and N represents the total number of spatial grid points in the area 20°S–20°N, 129.375°E–84.375°W. The rescaling factor is 0.19 °C, which is equal to the RMSE of the analysis SST.

Instead of adding random perturbations as in Cai et al. (2003), we superpose different random perturbations onto the analysis state to give different initial states in every breeding process and evaluate the corresponding NLLVs, which may contribute to the diversity of BVs and NLLVs. From the physical meaning of NLLVs, we determine that the corresponding time of each group of NLLVs is the moment at which the breeding process terminates. This is different from the definition of Tang and Deng (2011), who chose the initial time at which the random initial perturbation was added to the reference state, as the corresponding time for BV, which is unreasonable because BGMs (i.e. BVs and NLLVs) correspond to the backward Lyapunov vectors and are designed to simulate the initial analysis errors (Legras and Vautard 1996).

The parameters chosen above have some arbitrariness. Therefore, we test how much the NLLVs are affected by the parameters of the breeding process in the ZC model. Firstly, we want to identify how many breeding cycles are required for the breeding process. A sufficient number of breeding cycles ensures that the initial random perturbation can be fully developed to the fast growth directions. In order to explain this problem, we calculate the changes in the growth rate of different NLLVs with increasing number of breeding cycles (only displaying NLLV1 in Fig. 4a) and find that the growth rate of different NLLVs can reach the statistically stable stage in 12 cycles. The same result is obtained for other NLLVs. Therefore, we specify that every breeding process is made up of 12 breeding cycles. The growth rates of the first 10 NLLVs at the 12th cycle are shown in Fig. 4b. These growth rates are all greater than 1, which indicates that at least the first ten NLLVs are the error growth directions. The growth rate and hence importance of the NLLVs gradually decreases from NLLV1 to NLLV10.

We now explore the robustness of the NLLVs using different initial random perturbation seeds for the above breeding parameters. Figure 5 shows scatter diagrams of the spatial correlation of the SSTA field of the first three NLLVs evolved from two groups of different initial perturbation seeds but under the same breeding parameters. There are 3000 cases in each diagram, which correspond to 3000 different states. For the NLLV1, 60% of the absolute values of the spatial correlation coefficients are greater than 0.6 (Fig. 5a), which suggests that the sensitivity of NLLV1 to the initial perturbation seeds is small but not negligible. However, for the subsequent NLLVs, such as NLLV2 (Fig. 5b) and NLLV3 (Fig. 5c), the spatial structures of the NLLV become more sensitive: the corresponding percentage decreases from 14% of NLLV2 to 2.7% of NLLV3 and is smaller still for even higher numbered NLLVs. Compared with NLLV1, the subsequent NLLVs are more sensitive, which is one of the instantaneous features of the NLLVs. The nonlinearity of the dynamical system contributes to the sensitivity of the NLLVs to the initial random perturbation seeds. This sensitivity shows the infeasibility of checking the pattern correlation of NLLVs for each case to discuss the influence of breeding parameters. Therefore, we will focus on the statistical features of the NLLVs to explore the sensitivity of NLLVs to different breeding parameter sets. The statistical features of the NLLVs can be captured by their empirical orthogonal functions (EOFs).

3.2.2 *Sensitivity of the statistical features of NLLVs to the breeding parameters*

As mentioned above, it is important when calculating the NLLVs to choose appropriate breeding variables. Therefore, we use different combinations of variables as the breeding variable set to test the sensitivity of NLLVs to this choice. Here, we run four experiments: (1) the reference configuration experiment using TO, UO, VO, H1; (2) using just TO; (3) using TO, H1, oceanic depth averaged zonal current (U1) and oceanic depth averaged meridional current (V1); (4) TO, UO, VO, H1, U1, V1. The other parameters of the breeding process are the same as

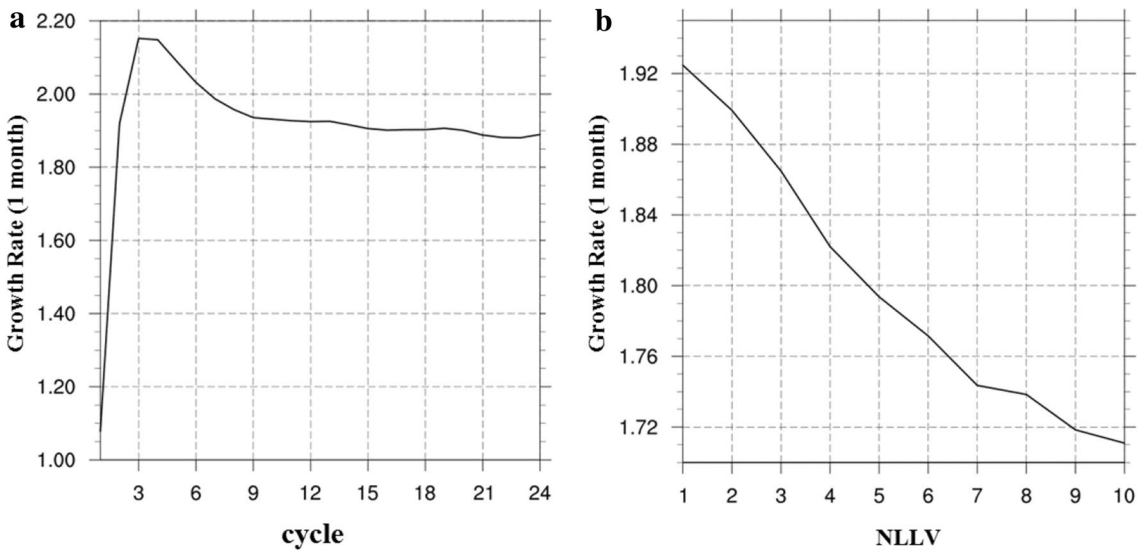

Fig. 4 The growth rate of the SSTA field of the NLLV1 as a function of the number of breeding cycles (**a**) and the growth rate of the first ten NLLVs through 12 breeding cycles (**b**). Here, the error growth rate is the average from the 408.5th to 3408.5th months. **a** Shows that the growth rate of the leading NLLV levels off first 24 breeding cycles. **b** Shows that the first 10 NLLVs are all directions of error growth

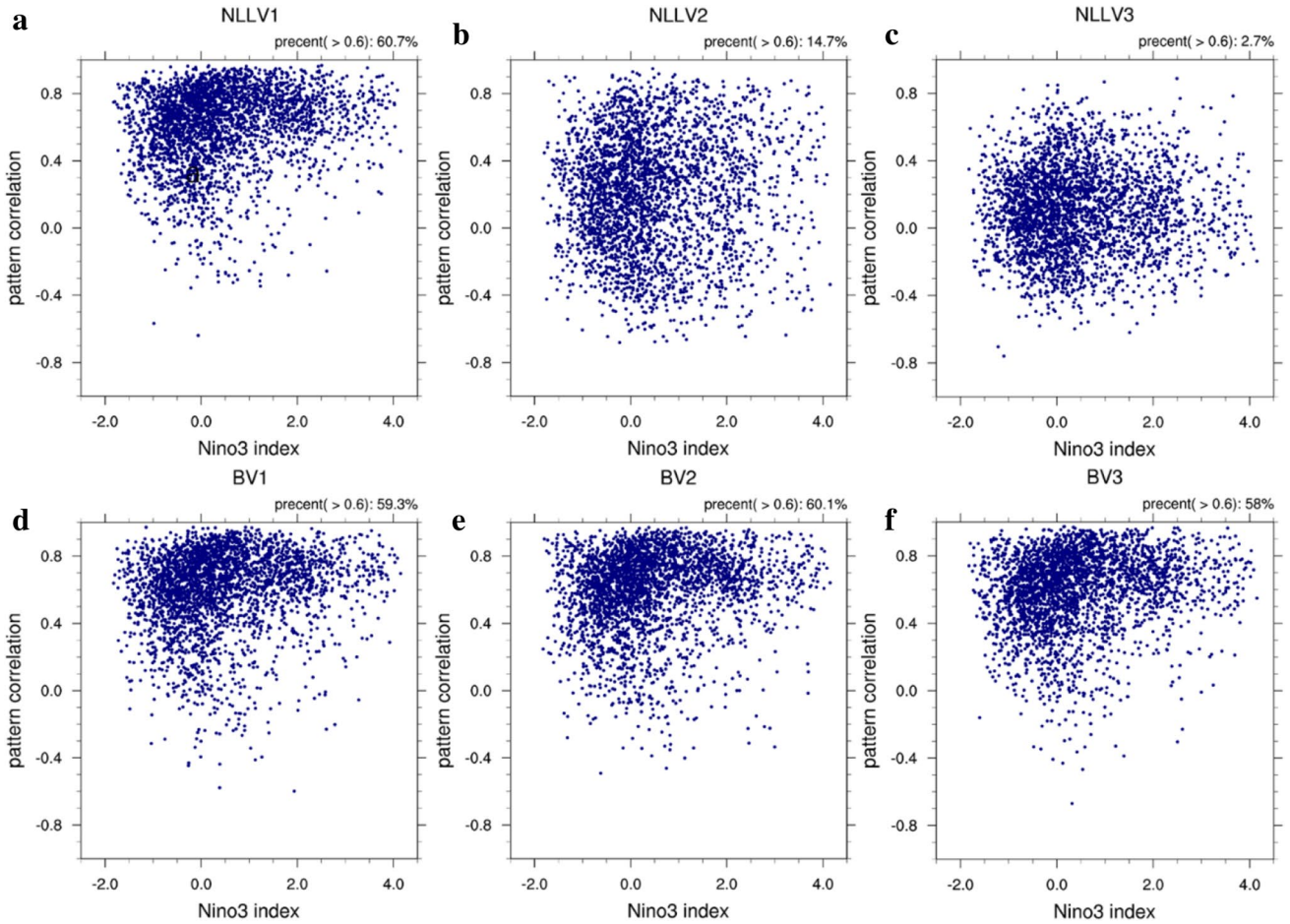

Fig. 5 Scatter diagrams showing the pattern correlations between the SSTA fields of NLLVs using two different initial random perturbations for every breeding process. **a** NLLV1, **b** NLLV2, **c** NLLV3. The corresponding pattern correlations are also shown for **d** BV1, **e** BV2 and **f** BV3. The abscissa is the Niño 3 index of the background ENSO events. The ordinate is the pattern correlation coefficient. The first three NLLVs corresponding to 3000 initial conditions are shown

for the reference configuration experiment. We compare the structure and corresponding explained variances of EOFs of the SSTA field of NLLVs from the 408.5th to the 3407.5th month.

Table 1 shows the average and standard deviation (SD) of explained variances for the EOF patterns of different NLLVs from the different variable sets. Compared with the average, the deviations are very small, which illustrates that the proportions of variances explained are nearly equal using different breeding variable sets. The variance explained by the first few EOF patterns of the NLLV1 is larger than that of the subsequent NLLVs. For example, the percentage of total variance explained by the first three EOFs of NLLV1 is 60.6%, that for NLLV2 is 47.5%, and that for NLLV3 is 35.4%. With the increase in the number of orthogonal directions, the variance explained by an equal number of EOFs of the higher NLLVs decreases, which shows that the NLLV1 is the dominant mode that is relatively less affected over time, but that the subsequent NLLVs cannot be completely described by one or a few dominant modes. The higher NLLVs have a certain randomness over time.

Table 1 Average explained variance and corresponding standard deviation for different EOFs of different NLLVs from different breeding variable groups

	EOF1	EOF2	EOF3
Explained variance			
NLLV1	41.227	10.590	8.829
NLLV2	21.568	14.716	11.179
NLLV3	14.580	10.939	9.882
Standard deviation			
NLLV1	0.394	0.132	0.061
NLLV2	0.327	0.351	0.160
NLLV3	0.542	0.258	0.233

The average and SD of the correlation coefficients between the corresponding spatial structures of the first

Table 2 Mean and standard deviation of correlation coefficients for the leading EOFs of the first three NLLVs between the reference parameter set and other breeding variable groups

	EOF1	EOF2	EOF3
Correlation			
NLLV1	0.999	0.999	0.999
NLLV2	0.996	0.993	0.996
NLLV3	0.982	0.868	0.825
Standard deviation			
NLLV1	1.56E−05	0.000551	0.000317
NLLV2	0.0018	0.0043	0.0016
NLLV3	0.0026	0.0774	0.0851

few EOFs of other parameter sets and that of the reference parameter set are shown in Table 2. The average correlation coefficients can reach 0.8 or more for the first few EOF patterns of the first few NLLV. The large mean and small SD of the correlation coefficients demonstrate that the patterns of EOFs of NLLVs from different breeding variable groups are very similar. Therefore, from the perspective of the explained variance and the spatial correlation coefficient of the corresponding EOF, the NLLVs are not sensitive in a statistical sense to the choice of breeding variable group. Meanwhile, the NLLVs other than NLLV1 are less and less explained by the first few EOF modes and include a larger random component.

Similarly, we choose different scaling factors S (1: the entire field; 2: only the Niño 3 (150°W–90°W, 5°S–5°N) area; 3: only the Niño 4 (160°E–150°W, 5°S–5°N) area; 4: the Niño 3 and Niño 4 areas), different scaling amplitudes [(50, 75, 100, 125, 150%)×0.199 °C] and rescaling intervals (1–4 months) and calculate the correlation of the structure and explained variance of the EOFs of the SSTA field of the NLLVs (not shown). Comparing the explained variances, averages and SDs of correlation coefficients for different breeding parameter sets, we find that there is very high consistency between these different parameter sets and the reference parameter set. Therefore, the structures of NLLVs are statistically very similar for different breeding parameter sets.

However, the variances explained by the first few EOFs of the later NLLVs (such as NLLV4, 5, etc.) become smaller with similar magnitude, so cannot be distinguished, which make it difficult to judge the similarity of the NLLVs structures statistically. Considering that the NLLVs can be used as ensemble perturbations for ENSO ensemble prediction and that the subspace made up of ensemble perturbations should involve the direction of analysis errors to ensure the effectiveness of ensemble forecasts (Toth and Kalnay 1993, 1997), we check the relationship between the subspaces composed of the first few NLLVs and the analysis errors. In this paper, we constructed the analysis data with the EnKF assimilation method under the perfect assumption and can acquire the analysis error by calculating differences between analysis data and true data. Referring to the Perturbation versus Error Correlation Analysis (PECA) proposed by Wei and Toth (2003), we obtain the correlation coefficient between the subspaces consisting of NLLVs and the analysis errors of SSTA at the same time through multiple linear regression methods. The square of this coefficient can be considered as the proportion of variance explained by the subspace constructed from the first few NLLVs to the analysis error. The correlation coefficient at each time is calculated by solving the maximum correlation between $\boldsymbol{Y} = \sum_{i=1}^{k} a_i \boldsymbol{NLLV_i}$ and $\boldsymbol{Y}_0$, where $\boldsymbol{Y}_0$ represents the analysis error of the SSTA field, the a_i are undetermined parameters and k is the number of selected first few NLLVs. To obtain $\boldsymbol{Y}$ at each time, we determine a_i by the least squares method. Using different breeding variable sets, the averages of the coefficients of different states (3000 cases) for different numbers of NLLVs are shown in Table 3. The relationship between the subspace and the corresponding analysis error is similar for different breeding variable groups. For other different parameter sets, the values are also consistent (not shown). Therefore, the NLLVs from different parameter sets or random perturbations are closely connected with the analysis error and this relationship is stable.

The instantaneous relationship of the NLLVs from different initial random perturbation seeds and different parameter sets, implies some sensitivity of the NLLVs, especially the subsequent NLLVs (NLLV2, NLLV3…), to the nonlinear evolution of the dynamical system over time. The subsequent NLLVs are more sensitive than NLLV1, which can be understood as the diversity of instantaneous NLLVs over time, which may contribute to the improvement of ensemble prediction. However, statistically, the NLLVs from different breeding parameter sets have great similarity in terms of the structure and explained variance of the EOFs. The relationship of the subspace of the first few NLLVs to analysis error is also similar. Thus, the features of NLLVs from different breeding parameter are similar and stable.

Table 3 Average correlation coefficient of the subspace composed of the leading few NLLVs and the corresponding analysis error for the 3000 samples for different sets of breeding variables

Coefficient	TOUOVOH1	TO	U1V1TOH1	U1V1TO UOVOH1
NLLV1	0.259	0.264	0.255	0.261
NLLV12	0.399	0.387	0.406	0.402
NLLV123	0.479	0.483	0.468	0.474
NLLV1234	0.534	0.542	0.532	0.536
NLLV12345	0.574	0.581	0.569	0.570

Therefore, in the remainder of the paper, results are presented with the breeding parameters set as: the L2 norm (the entire field), with rescaling size equal to the RMSE of the analysis SSTA field (0.199 °C), with one month for a breeding cycle and SSTA UO VO H1 as the breeding variables to set the orthogonality of the perturbations at the end of every breeding cycle.

4 Growth rates and modes of NLLVs

Previous research (Cai et al. 2003; Yang et al. 2006, 2008; Tang and Deng 2011) has produced the important results that the growth rate and mode of BVs are functions of background ENSO phase and season. The maximum BV growth rate occurs between the two extreme phases of ENSO episodes and the extreme centers of the BV mode vary with ENSO phase (Cai et al. 2003; Yang et al. 2006). Considering NLLVs as the nonlinear extensions of LVs in a multidimensional context, we conjecture that there is a relationship between the ENSO phase and the growth rate or modes of the different NLLVs. Therefore, having determined the configuration of the breeding process, in this section we will explore the features of NLLV modes and their variations with initial state, season, and ENSO signal over a 250-year period, starting at year 34 of model time.

4.1 Variations of NLLV growth rate

NLLV growth rate is measured as the ratio of the SSTA field of the NLLV at the end of the breeding interval (one month) compared with its initial amplitude (i.e., the rescaling factor) and it has units of per month. The growth rate is just the relative increment in a breeding cycle of 1 month, which is different from the time span used by Cai et al. (2003). Figure 6a displays the percentage of cases for which the growth rates of the first three NLLVs rank at position i in the 3000 sample pool. In this figure, we find that although the NLLV1, defined as the statistic fastest growth direction, is fastest ($i=1$) the greatest percentage of the time, the percentages of the next two NLLVs together reach 60%. Figure 6b shows the growth rates of the first three NLLVs in the steady growth period of the breeding process for different seasons. The growth rates of the first three NLLVs, in rough agreement with the variation of the optimal error growth rate for the BV from Cai et al. (2003), are larger in summer and fall than in other seasons. This may be because of the stronger convectional heating in summer and the fact that ENSO events tend to strengthen during the fall season. The growth rates in late spring rapidly increase, which may correspond to the rapid decrease of the prediction skill in spring (i.e. the spring prediction barrier). The change of amplitude of the growth rate of late spring indicates the unstable part of ENSO that is difficult to predict. The different NLLVs have similar seasonal variations in growth rate although there are some differences in the values of the growth rates. The growth rates of subsequent NLLVs in some seasons are even larger than that of the NLLV1, which indicates the importance of subsequent NLLVs at some times. In Fig. 6c, the NLLV2 has the highest probability to be the fastest growth direction in the summer, especially in June and July, which further confirms that the first NLLV is not always the fastest growth direction over a short time interval, although statistically NLLV1 has the fastest growth rate. In the spring, the percentage of the NLLV2 as the fastest direction rapidly increases, which corresponds to the spring barrier. Therefore, from this growth rate perspective, we cannot discard the subsequent NLLVs and just choose the NLLV1 or BV and it is necessary to consider the subsequent NLLVs to describe the multidimensional error growth space of the ZC model.

We want to identify the relationship between the growth rates of these subsequent NLLVs and the background ENSO phase. Thus, we will check the growth rate of the NLLVs at different ENSO phases. The dependence of the growth rates of BVs on ENSO phase has been addressed in Cai et al. (2003) and Yang et al. (2006). They found that a neutral or onset/breakdown stage of an ENSO event tends to have a large error growth about 3–4 months prior to the peak phase, whereas error growth is often small in an ENSO peak phase. Tang and Deng (2011) also pointed out similar characteristics of BV growth rate in a hybrid coupled ENSO model of the 120 year between 1881 and 2000. In addition, Tang and Deng (2011) showed that the BV growth rate is smaller during El Niño than La Niña events. Here, we follow Cai et al. (2003) and divide the background ENSO events into 24 categories. The boundaries of the 24 bins are based on the Niño 3 index of the control run and its temporal trend. Table 4 summarizes the lower and upper boundaries of the bins in terms of the Niño 3 index and its temporal tendency. The choice of limits means that bins 12 and 13 represent the warmest SST anomaly phase of the composite ENSO event. Bins 5–20 have a positive Niño 3 index and the remaining bins correspond to a negative index. Figure 6d displays the composite mean of the growth rate of the first three NLLVs as a function of the background ENSO phase. It is clear that the NLLVs tend to have a larger growth rate in the developing stage of the ENSO positive phase. In the mature stage of the ENSO positive phase, the growth rate is the smallest. Besides, there are some differences in the amplification of the growth rates of the ENSO positive and negative stages. In the negative phase, the growth rate of the NLLV1 is lower compared with the NLLV2 and NLLV3, which shows the importance of the subsequent NLLVs' directions for describing the error growth subspace, particularly in the ENSO negative phase. Therefore, the instabilities related to ENSO

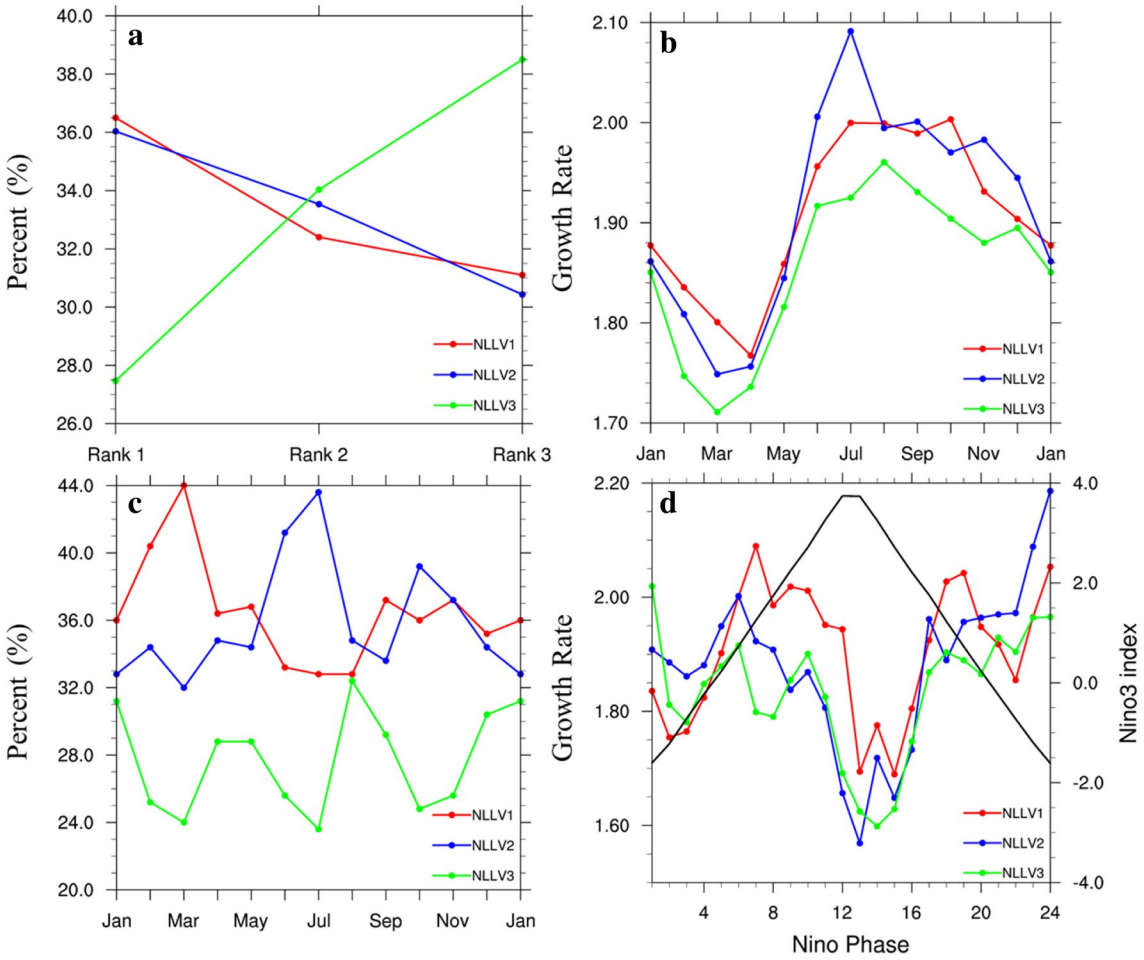

Fig. 6 Percentage of the first three NLLVs in the position of the corresponding rank (**a**), the growth rates of the first three NLLVs for different seasons (**b**), the percentage of the first three NLLVs as the fastest growth direction for different seasons (**c**) and the average growth rate of the first three NLLVs as a function of the ENSO phase (**d**). The black curve of **d** is the Niño 3 index of the composite background ENSO cycle corresponding to the right vertical axis. The growth rate $\boldsymbol{\gamma}$ is calculated as the scaling factor in the final breeding cycle of the breeding process

Table 4 Lower and upper limits of the 24 Niño3 bins for the composite ENSO event

	Bin no.											
	1	2	3	4	…	12	13	…	21	22	23	24
Lower limit	<-1.5	-1.5	-1	-0.5	…	3.5	3.5	…	-0.5	-1	-1.5	<-1.5
Upper limit	-1.5	-1	-0.5	0	…	>3.5	>3.5	…	0	-0.5	-1	-1.5
d(Niño3)/dt	>0	>0	>0	>0	>0	>0	<0	<0	<0	<0	<0	<0

are not only determined by one direction such as the NLLV1 but are also influenced by the subsequent NLLVs.

Decadal and interdecadal variations in ENSO variability exist as shown in Fig. 3. ENSO variability is weak during the period from the 700.5th to 1700.5th months and is strong from the 2000.5th to 3000.5th months as determined by the Niño 3 index. It is interesting to examine the temporal variations of the NLLVs growth rate on the decadal/interdecadal scale. Figure 7 shows variations in the NLLVs growth rate from the 408.5th to 3408.5th month; a 48-month (4-year) running average has been applied to highlight interannual or longer signals. Forty-eight months is the significant period of the ENSO cycle in the ZC model. Scrutiny of Fig. 7 reveals that the differences between the growth rates of the NLLVs also have decadal/interdecadal variation. NLLV2 or NLLV3 as well as NLLV1 all have the potential to become the fastest growing direction of the leading NLLVs in some periods. The Niño 3 index indicates that the ENSO has

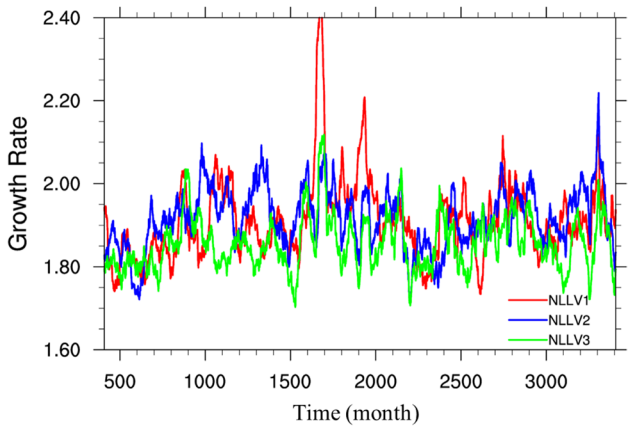

Fig. 7 Variation in the growth rate of the first three NLLVs. A 48-month running mean has been applied to the rate and index to highlight interannual and longer signals

different characteristics in the periods 1000.5–1500.5th and 2000.5–2500.5th months: the former represents an irregular stage and the latter is the regular stage of the ENSO cycle. The two stages have different NLLV growth rates: the growth rates in the irregular period are higher than in the regular stage. The regular ENSO cycles contribute to increasing predictability and the irregular cycles give decreased predictability. The variability of the NLLVs growth rate at various time scales is more obvious in the wavelet analysis shown in Fig. 8. The local wavelet power spectrum of the NLLV1 growth rate clearly indicates that significant periods were localized in time and varied from 180 to 240 months from the 1000.5th to 2200.5th months, which agrees with the Niño 3 index wavelet power characteristics.

The wavelet power spectrum analysis for the NLLVs growth rate and Niño 3 index also reveals similar spectral characteristics between the NLLVs growth rate and ENSO variability, suggesting a connection of the growth rates of different NLLVs with the ENSO background. There are some differences in the time and duration of the most significant frequencies of variation of different NLLVs, which further confirms the diversity of the increasing error directions represented by the NLLVs. Therefore, different first NLLVs, including at least NLLV1, NLLV2, and NLLV3, actually have a close relationship with the ENSO process and have sufficient diversity to describe the different aspects of ENSO.

4.2 ENSO NLLV modes

Cai et al. (2003) pointed that the BV mode exhibits a large-scale spatial pattern somewhat similar to ENSO over much of the equatorial Pacific basin. Yang et al. (2006) found the BV has similar behavior to the forecast error field. Therefore, in this section we want to show whether the NLLV structures have a temporal dependence on the background ENSO flow. Thus, we randomly chose a period that ranges from one ENSO negative mature phase to the next negative mature phase and examine the zonal and temporal snapshots of the SSTA field of NLLVs along with the background SSTA (as shown in Fig. 9). Figure 9 reveals that the structure of the first three NLLVs (color shading) is dependent on the

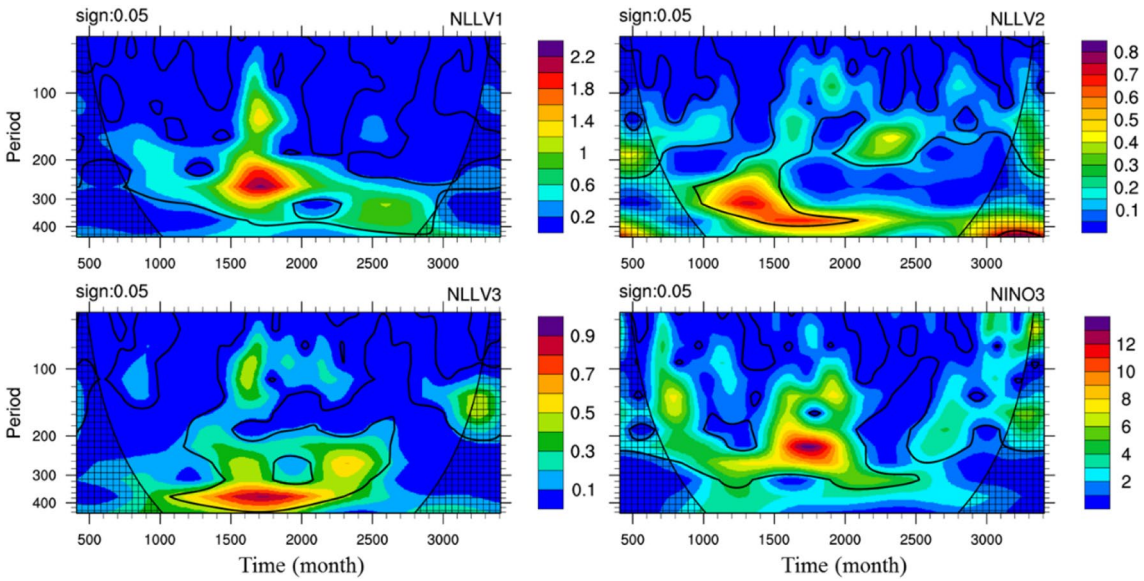

Fig. 8 Morlet wavelet power spectra of the NLLV growth rates and the Niño 3 index. The thick contour encloses regions of greater than 95% confidence using a red-noise background spectrum. The solid smooth curves in the bottom left and right corners indicate where edge effects become important

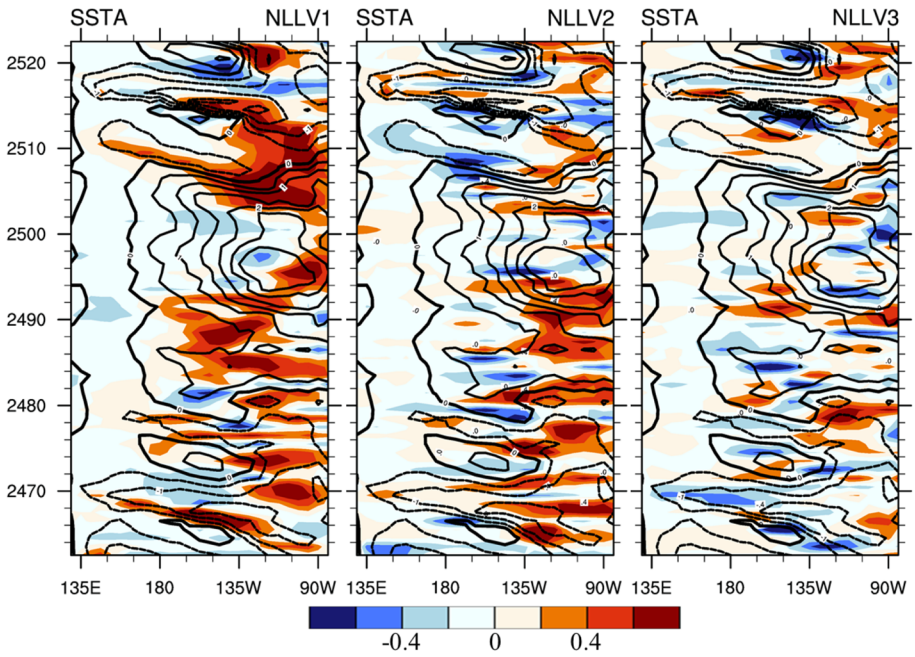

Fig. 9 Evolution of SSTA structures (contour interval 0.5 units; solid for positive and dashed for negative) and corresponding SSTA fields of the first three NLLVs (shaded) for a particular randomly chosen ENSO cycle. Here the displayed fields are averaged over the region from 5°S to 5°N

background SSTA fields (contours). The NLLVs often have centers of extreme values in the area where the background SSTA field varies rapidly with time, such as the eastern Pacific. When it is the developing stage of an El Niño or La Niña, the SSTA field of the NLLVs has more extreme centers and extends from the eastern Pacific to the western Pacific. During the El Niño mature phase, the NLLV structures are weaker and lie mainly in the east Pacific. From the La Niña to El Niño phase (from the 2466.5th to 2490.5th month), the extreme centers of NLLVs in the western Pacific gradually decay but that in the eastern Pacific is maintained and enhanced, which agrees with the development of the background fields. Compared with the NLLV1, the subsequent NLLVs such as NLLV2, NLLV3 have finer structure, for example during the beginning of the El Niño phase (at the 2494.5th month), NLLV2 and NLLV3 have a stronger signal in the central and eastern Pacific, which contributes to the development of the El Niño phase. Therefore, NLLVs are dependent on the background flow and have different patterns at different ENSO phases, which is consistent with the behavior of BVs. The subsequent NLLVs besides NLLV1 can also represent the instability structure associated with ENSO and contain finer scale information. They also contribute toward the error growth subspace of the multidimensional system.

As mentioned in the Sect. 3.2, the statistical properties of the NLLVs are stable and to some extent insensitive to the choice of the breeding parameter. To explore the physical significance of the statistical structure, the EOFs of the SSTA field of each of the NLLVs are displayed in Fig. 10. The different EOF patterns of the NLLVs have different numbers of extreme centers. The EOF1 of NLLV1 has a uniform structure; the EOF2 has a dipole structure and the EOF3 is tripolar. The first three EOF patterns of the NLLV1 have physical significance related to ENSO. The EOF1 pattern represents the uniform ENSO-like structure with a large-amplitude signal in the equatorial central and eastern Pacific, which is similar to the final evolved singular vector and is closely related to the delayed-oscillator mechanism (Tang and Deng 2011). The EOF2 pattern is similar to the nonlinear forcing singular vector (NFSV) of the growth-phase predictions (Duan and Zhao 2014), which also has a zonal dipole structure and positions of the extreme centers that are consistent with those of the NLLV1 EOF2. Duan and Zhao (2014) pointed out that this NFSV pattern is responsible for the prediction error of the corresponding El Niño event in the ZC model. The tripole structure of the EOF3 pattern is more or less consistent with the EOF structure of the subsurface ocean temperature (Zhang et al. 2017). The EOF structures of different NLLVs have certain similarities. For example, the EOF1 of the NLLV1 and the EOF1 of the NLLV2 both have the single structure in all fields. These similarities are because all the NLLVs are associated with the background ENSO evolution and represent the flow-dependent error growth directions. However, there are also differences between EOF1s for different NLLVs. The single structures have different intensity and extent. The results are similar for other EOF modes. The differences are due to the nonlinearity of the dynamical system and show the diversity of the NLLVs.

Considering that the background ENSO states have a significant difference in the two spans: the 700.5th–1700.5th and 2000.5th–3000.5th months (shown in the Fig. 3), the first three EOF of first three NLLVs have some differences

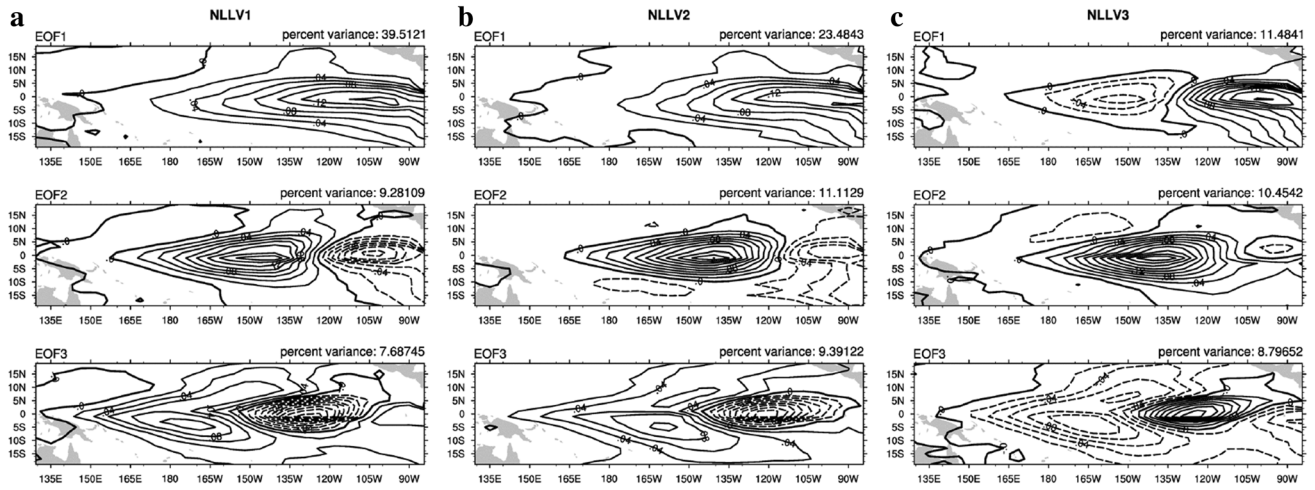

Fig. 10 The first three EOF structures of the SSTA fields of the first three NLLVs (contour interval 0.02 units; solid for positive and dashed for negative): NLLV1 (**a**), NLLV2 (**b**), NLLV3 (**c**)

in structures and explained variances. The difference exists in the growth rate of the NLLVs (as shown in Fig. 7).

These figures demonstrate that the different directions of the first few NLLVs represent the growth directions and are related to the ENSO evolution. The directions of the different NLLVs all have the potential to be the fastest direction at a particular instantaneous state. The subsequent NLLVs are random to a certain extent; this contributes to the diversity of the first few NLLVs. Therefore, using different NLLVs is helpful to describe the subspace of the error growth. We are confident that NLLVs will perform better as ensemble perturbations than BVs.

5 Advantages of NLLVs over BVs

As mentioned above, in theory the NLLVs have some advantages over BVs. The orthogonalization of the breeding process means that the NLLVs can represent different error growth directions and include greater diversity than the BVs. As shown in Fig. 5, the subsequent NLLVs (Fig. 5a–c) are somewhat more random than the BVs (Fig. 5d–f). Therefore, the subspace constituted by the first few NLLVs should have a higher correlation with the analysis error than that of the BVs. Figure 11 displays the correlation coefficients between the subspace of NLLVs and BVs against the analysis error by the PECA method. The coefficient is the average of 3000 cases, corresponding to different initial states from the 408.5th to 3407.5th months. The different numbers of vectors represent the different dimensions of the subspace. Figure 11 shows that the coefficient of the NLLVs is always larger than that of the BVs for different dimensional subspaces. The difference reaches almost 0.1 with five vectors. The

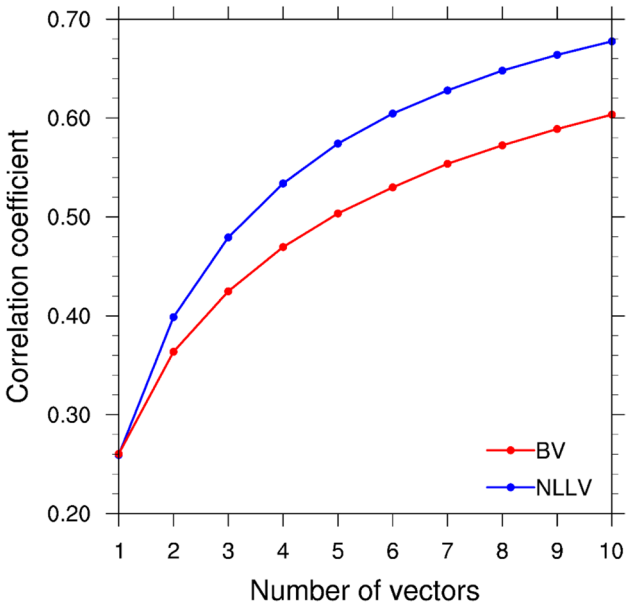

Fig. 11 Average correlation coefficient between the subspace composed of the first few NLLVs (blue line) and BVs (red line) and the corresponding analysis error for the 3000 cases. The number of vectors on the horizontal axis represents the different numbers of NLLVs or BVs used to construct the subspace

difference is not due to the similarity of BVs, because the orthogonalization of BVs cannot change the subspace consisting of BVs. The difference is because the different NLLVs represent different error growth directions which have physical meaning. The orthogonalization of the breeding process ensures the different NLLVs adequately resolve the physics. Therefore, the subspace consisting of NLLVs can better and more effectively capture the analysis error than that of an equal number of BVs.

In fact, the orthogonality contributes to the effectiveness of NLLVs in describing the error growth subspace. However, the orthogonality of NLLVs holds in a whole-regional sense and does not guarantee the mutual independence of local NLLVs. The diversity of local perturbations impacts the ensemble skill (Wang and Bishop 2003). Here, we want to identify whether the local dimensionality of the NLLVs is higher than that of the BVs.

We calculate the local dimensionality of the NLLVs or BVs following Patil et al. (2001). We chose 5×5 grid cells, roughly 1000 km$\times$2500 km, as the local region and regard it as the local 25-dimensional vector. The total number of vectors (NLLVs or BVs) is k. The k local column vectors form a $25\times k$ matrix, B. The $k\times k$ covariance matrix of B is $C = B^T B$, where B^T is the transpose of B. C is non-negative definite and symmetric, so its k eigenvalues λ_i are non-negative. Therefore, the singular values of B are $\sigma_i = \sqrt{\lambda_i}$, and the local dimensionality of vectors is defined as:

$$\psi\left(\sigma_1, \sigma_2, \ldots, \sigma_k\right) = \frac{\left(\sum_{i=1}^{k} \sigma_i\right)^2}{\sum_{i=1}^{k} \sigma_i^2}, \tag{3}$$

where ψ returns a real value between 1 and k. Here, k is chosen to be 5.

In Fig. 12, we show the spatial distribution of the local dimensions of NLLVs and BVs. The local dimensionality is calculated at each spatial point on the grid and colored blue for lower values and red for larger values. As shown in Fig. 12, the local dimensions of NLLVs are higher than those of BVs, and this is not sensitive to the grid size or the number of vectors k. The difference is up to 0.8 over almost the whole region and becomes larger when the grid number increase. The local dimensions of NLLVs are higher in the western and eastern Pacific than in the central tropical ocean, which may be because the western and eastern areas are the regions of varying SSTA. Therefore, the NLLVs have more diversity than the BVs whether in a whole-region sense and locally, which is beneficial for the prediction skill of NLLVs as the ensemble perturbations.

6 Application of NLLVs in ensemble prediction

In this section, we apply the first few NLLVs as ensemble perturbations to predict ENSO and demonstrate the potential benefits in the context of the perfect model scenario. Four groups of forecast experiments are designed. In addition to the control experiment from the single analysis state of the EnKF assimilation method, we perform three other ensemble prediction experiments whose ensemble perturbations are produced separately by the NLLV, BV, and random schemes. These perturbations are added and subtracted from the analysis states. As mentioned above, the NLLVs are generated through breeding processes. The breeding processes contain twelve breeding cycles and the length of a breeding cycle is 1 month. The parameters of the breeding process for BVs are the same for NLLVs. The orthogonalization process is included in each breeding cycle for the NLLVs but not for the BVs. The ensemble perturbations of the three methods have the same size as those of the analysis errors of the SSTA field in L2 norm. The number of ensemble members is ten using the five directions from the BV, NLLV and random vectors (positive–negative pairs). Five modes are chosen because the first five NLLVs can explain the majority

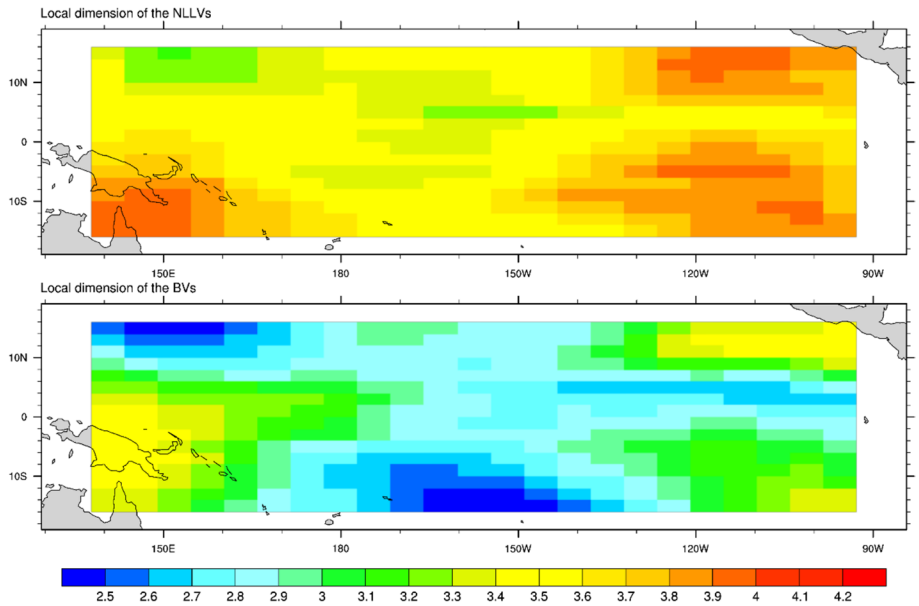

Fig. 12 Local dimensionality of the fore five NLLVs (upper) and five different BVs (lower). The local regions are made up of 5×5 grid cells. The local dimensionality is the average of 3000 cases from the 408.5th to the 3407.5th month

of the analysis errors at reasonable computational cost. The ensemble members are integrated for 48 months, almost equal to the period of the ENSO cycle in the ZC model. The initial forecast time is every month over a 250-year period and there are 3000 forecast cases in total. We check the prediction skill of the Niño 3 index of the different schemes with regard to the ensemble mean and probability prediction.

6.1 Skill of the ensemble mean

The overall prediction performances of the ensemble mean can be measured through mean square root error (RMSE) and pattern anomaly correlation (PAC) (Buizza et al. 2005). These are expressed as:

$$RMSE(t) = \sqrt{\frac{\sum_{i=1}^{N} \left(pre_i(t) - tru_i\right)^2}{N}}, \tag{4}$$

$$PAC(t) = \frac{\sum_{i=1}^{N} \left(pre_i(t) - \overline{pre(t)}\right) \times (tru_i - \overline{tru})}{\sqrt{\sum_{i=1}^{N} \left(pre_i(t) - \overline{pre}\right) \times \left(pre_i - \overline{pre}\right)} \times \sqrt{\sum_{i=1}^{N} (tru_i - \overline{tru}) \times (tru_i - \overline{tru})}}, \tag{5}$$

$$\overline{pre(t)} = \frac{\sum_{i=1}^{N} \left(pre_i(t)\right)}{N}, \ \overline{tru} = \frac{\sum_{i=1}^{N} \left(tru_i\right)}{N}$$

where t is lead time, i represents the number of samples used to calculate the forecast skill. N is the total number of objects considered; pre_i is the predictand and tru_i represents the corresponding analysis quantity. $\overline{pre}$ is the average of all pre_i and $\overline{tru}$ is that of all tru_i.

We focus on the prediction skill of the Niño 3 index. Figure 13a, b show the RMSE and PAC of the Niño 3 index, respectively, as a function of lead time. The corresponding measurements from the control forecasts are also shown for comparison. The ensemble averaging significantly outperforms the single control forecast as a whole, although different ensemble methods, because of their distinct initialization schemes, have different forecast skills. For the first few months (about 5 months), ensemble averages are indistinguishable from the control forecasts. The initial time span can be considered as a linear stage, during which the pairs of positive and negative perturbations cancel each other out almost completely and the average results of the pairs are almost equal to the control forecast results. However, when the errors gradually increase and enter the nonlinear stage, ensemble averaging plays a much more important role in filtering nonlinearly to reduce error. In the nonlinear stage, the BV method evidently outperforms the random vector method in ensemble prediction skill, because of the representation of the analysis error directions by the BVs. Due to the assimilation cycles that generate the analysis states, non-growing error directions are reduced down to a low proportion and a significant fraction of the analysis errors are represented by

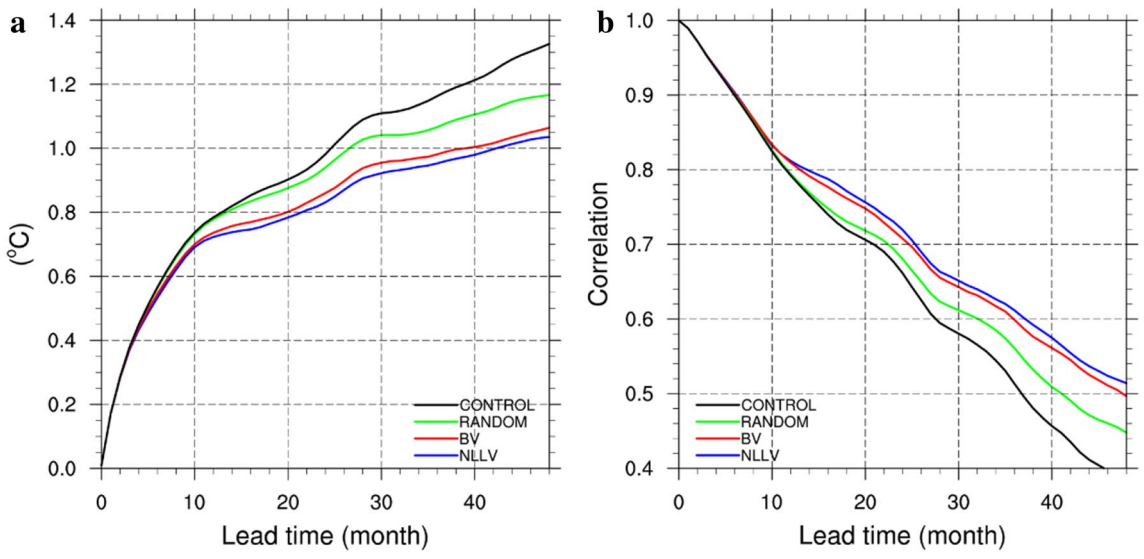

Fig. 13 RMSE (**a**) and mean correlation (**b**) of 3000 samples as a function of lead time for the control run (black line), random perturbation method (green line), BV method (red line), and NLLV method (blue line)

the growing error directions. Random perturbations that only include a small proportion of the growing errors describe the probabilistic distribution of analysis errors in the less efficient directions and have the worst ensemble prediction skill. The ensemble skill of the NLLVs is higher than that of BVs, which is due to the diversity of the NLLVs. NLLVs sample the analysis errors in more mutually orthogonal directions and can describe the probability distribution of the analysis errors more fully than the other two schemes. The subspace of the first NLLVs has better correlation with the fast-growing component of the analysis errors, and thus the NLLVs behave better than the traditional BV and random method, especially for long-range predictions. This point is proved by the PECA method.

6.2 Probabilistic forecast verification

The probability forecast can provide information about the predictability. Murphy (1988) pointed out that the spread of an ensemble distribution can in principle give an a priori indication of forecast skill. The smaller the spread, the higher is the prediction reliability and vice versa. Therefore, there is an inverse relationship between ensemble spread and the mean prediction accuracy for a statistically reliable ensemble system. The ensemble spread should be close to the error of the ensemble mean (Buizza et al. 2005). The ensemble spread is given as (Buizza and Palmer 1998; Zhu and Toth 2008):

$$Spread(t) = \sqrt{\frac{1}{N-1}\sum_{i=1}^{N}\left(pre_i - \overline{pre}\right)^2}, \tag{6}$$

where t represents the lead time, $\overline{pre}$ is the average value of the ensemble prediction and the $Spread(t)$ represent the standard deviations of the ensemble members.

Figure 14 shows the ratio between the ensemble spread and the RMSE of the Niño 3 index as a function of lead time for different perturbation schemes. At the lead time of 3 months, the Spread is larger than the RMSE for NLLV and BV ensemble schemes. The spread of the Niño 3 index of the random scheme is too low, because the random values in the Niño 3 region cancel each other out when added together. With increasing lead time, the ratio of the NLLV and BV schemes gradually reduces to less than 1. In this process, the ratio of the NLLV scheme is always larger than that of other schemes, which demonstrates that the NLLV scheme can more accurately describe the relationship between the Spread and RMSE. This is attributed to the NLLVs sampling the analysis errors in directions that are much less correlated than those used in the BV scheme.

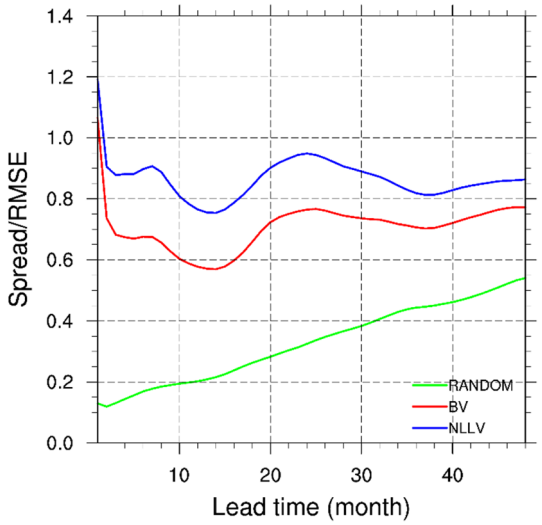

Fig. 14 Ratio of the ensemble member spread (represented by the averaged standard deviations of the model ensembles) and the RMSE of the ensemble mean shown as functions of lead time for different ensemble schemes: random perturbation method (green line), BV method (red line), and NLLV method (blue line). Values close to 1 represent good results

In ENSO prediction, we are interested in the prediction of the La Niña (cold events) and El Niño (warm events). There are a number of scalar accuracy measures for verification of probabilistic forecasts of dichotomous events, but by far the most commonly used is the Brier score (BS). Thus, we use the BS to verify the prediction skill of the two kinds of event. We define warm events as when the Niño 3 index is larger than 2.15 °C (the upper 10% range of the Niño 3 index series) and cold events as when it is less than −0.86 °C (the lower 10%). The BS can be defined as the mean square probability error (Wilks 2011):

$$BS = \frac{1}{N}\sum_{i=1}^{N}\left(f_i - O_i\right)^2, \tag{7}$$

where the index i denotes a numbering of the N forecast–event pairs; f_i is the prediction probability of the events occurring; if the event happens, the observation $O_i = 1$, and $O_i = 0$ if the event does not occur. In this form, the BS is anti-correlated with the skill of the forecast: a higher BS represent a less accurate prediction (Murphy 1973). The BS can take on values only in the range $0 \leqslant BS \leqslant 1$. Figure 15 shows the BS of warm and cold events evaluated for three methods as a function of forecast time. At the beginning of the first 5 months, the prediction ability of warm and cold events by the three methods is close. With increasing lead time, the ability of the NLLV and BV methods becomes increasingly clear. The BS of the NLLV method is always lower than for

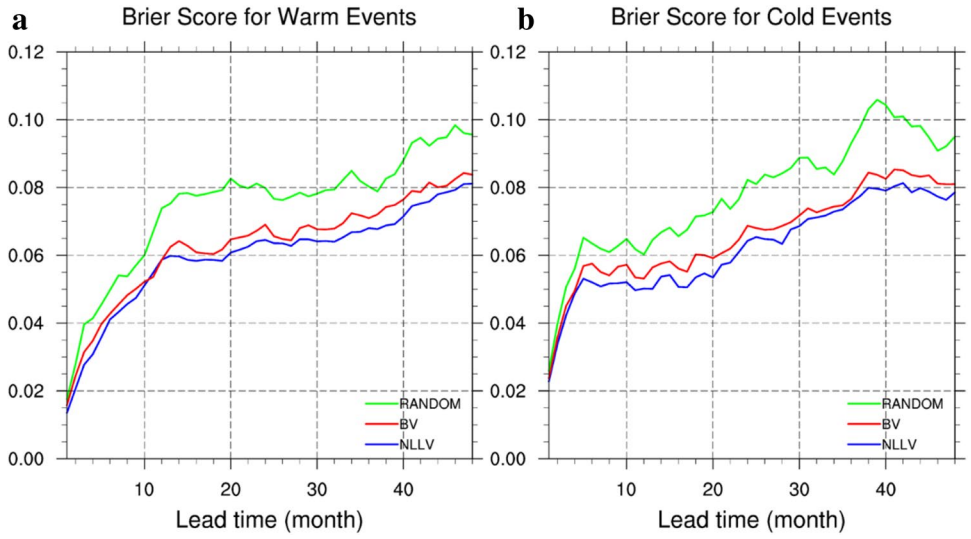

Fig. 15 Evolution of the Brier Score of warm events (**a**) and cold events (**b**) as a function of lead time for the NLLV, BV and random schemes

other methods. The NLLV method performs better in predicting warm and cold events than other schemes.

The diversity and the close relationship with the analysis error of NLLV contribute to its performance in ensemble prediction. Using the PECA methods, we check the relationship between the analysis error field and the different perturbation schemes for SSTA. We calculate the explained variance of the analysis error for the ensemble perturbations each month and obtain the square root of the explained variance as the correlation coefficient from the 408.5th to the 3407.5th month. The correlation coefficient of the NLLV scheme is 0.574 and that for an equal number of random perturbations is only 0.083, which indicates that the subspace made up of the first few NLLVs is more closely related to the analysis error than that of random vectors. The analysis error from the assimilation process consists of the background error from the background field and the random error from observations. The growing directions of the background error account for the important structure of the analysis error in the ZC mode. Because the breeding process is similar to the assimilation process, NLLVs represent the increasing directions of the dynamical system and have a close relationship with the background error through the breeding process. Compared with the BV method, the mutual orthogonality of NLLVs contributes to the diversity of the ensemble perturbation. Therefore, using the NLLVs as the ensemble perturbation can improve the prediction skill of ENSO in the ZC model, as proved by the experimental results.

7 Conclusions

In this study, we interpret NLLVs as extensions of the theoretical Lyapunov vectors and apply NLLVs to the ZC model to explore how to calculate the NLLVs, explore the NLLV characteristics, and evaluate the performances of the NLLV scheme for ENSO ensemble prediction in the perfect model environment. The NLLVs are a development of BVs. Through the breeding process, both the NLLV and BV can capture the growing directions of analysis errors from assimilation cycles. However, unlike the BV, the NLLV is periodically orthogonalized by the GSR process to separate various growing directions of the dynamical system. The continual orthogonalization in the breeding process ensures that the different unstable directions represented by NLLVs can develop sufficiently and be maintained. The mutually orthogonal NLLVs have greater diversity and higher independence than the BVs.

Before calculating the NLLVs in the ZC model, for closer consistency with the operational environment, we constructed the assimilation process using the EnKF method to generate the analysis data without considering the model error. Using this analysis data as the reference trajectory, we demonstrated the feasibility of NLLVs to facilitate ENSO studies in this near-operational prediction environment. The ZC model has no weather or other fast timescale instabilities. Therefore, we have little doubt in relating the growing structure identified with NLLVs to the background flow. We ran some experiments to illustrate the potential benefit of using NLLVs in this coupled model. We explored the characteristics of the spatial patterns and the growth rates of NLLVs.

We found that the instantaneous structures of NLLVs differ with the choice of breeding parameters and initial random perturbation seeds, especially the higher NLLVs (NLLV2, NLLV3,…). Due to nonlinear effects and the orthogonalization process, the subsequent NLLVs have a certain randomness. The randomness of the NLLVs contributes to the diversity of the NLLVs and guarantees the effectiveness of the subspace consisting of the first few NLLVs in describing the unstable directions of the ENSO dynamical process.

However, the statistical features of NLLV are insensitive to these breeding parameters, because all NLLVs represent the unstable directions of ENSO and are relative to the dynamical process of the background flow. The stability of the statistical properties is one of the NLLV advantages, which supports the application of NLLVs to the operational environment.

We have explored the characteristics of the spatial structures and growth rates of different NLLVs in the ZC model. Both the spatial structures and the growth rates of NLLVs (NLLV1 and the subsequent NLLVs) are related to the background ENSO events and seasonal cycle. The largest growth rates of NLLV1 and the subsequent first few NLLVs occur in boreal summer and fall. The growth rates of NLLVs are also strongly dependent on the background ENSO phase. The growth rates of the first few NLLVs are smallest at the mature stage of an El Niño event, while the largest error growth rates emerge during the ENSO neutral stages. In some phases of ENSO, the growth rates of other NLLVs (NLLV2, NLLV3…) may be larger than that of the NLLV1. In fact, the NLLV1 represents the statistically fastest growing direction. However, the other NLLVs have some probability of growing fastest. The first few NLLVs are also related to the background flow on the decadal/interdecadal time scale. The growth rates of the different NLLVs manifest different structural characteristics of the wavelet. The temporal variation of the NLLVs depends on the background flow. The extreme values of the NLLVs tend to be located at the temporal and spatial location where the background flow changes rapidly. Analyzing the first three EOF structures of the first three NLLV (the NLLV1, NLLV2, NLLV3) respectively, we find that the EOF structures from different NLLVs have some similarity because the NLLVs are all related to the background ENSO flow. The NLLVs have some advantage over BVs in terms of the relationship between the error growth subspace and the analysis errors. The NLLVs also have higher local dimensionality than the BVs.

We have conducted ensemble forecasting of ENSO using NLLVs as the ensemble perturbations in the ZC model. The NLLV scheme for ENSO ensemble prediction performs better than the BV and random approaches in terms of RMSE and PAC of the ensemble mean, the relationship of spread and RMSE, and the BS of warm and cold events. This may because the development of analysis errors can be effectively sampled by the NLLVs and the diversity of the NLLVs as ensemble perturbations are high. Therefore, the NLLV scheme is an effective method for generating ensemble perturbations to predict ENSO.

This study simply uses the ZC model without model error. This deficiency leads to a higher predictability limit in this paper than that of the real ENSO prediction. Therefore, we will apply the NLLVs to predict real ENSO events in future work. The ZC model is an intermediate coupled model which does not include realistic atmospheric transitions and weather scale variability. Therefore, we need to verify the sensitivity of NLLVs to the atmospheric noise in complex coupled general circulation models (CGCMs). In this paper, we find that the subspace consisting of the NLLV perturbations is closely related to the analysis errors. The largely explained ratio of the perturbations to the analysis errors contributes to the high prediction skill traditionally. However, low prediction skill occurs with large correlation coefficient in some cases in this experiment. The relationship of the coefficient between the subspace of the perturbations and the analysis errors and prediction skill is complex and uncertain. The relationship should be explored further. However, in this paper, the NLLVs are directly used as the ensemble perturbations. When increasing the member of perturbations, the invalid direction from the subsequent NLLVs reduce forecast skill. Therefore, we need to choose the appropriate number of NLLVs as the perturbations.

Acknowledgements We would like to thank Dr. Yaokun Li for providing the Zebiak–Cane model and Dr. Nan Xing for instructions on how to run the model. This research is supported by the National Natural Science Foundation of China (NSFC) Project (41375110), the National Natural Science Foundation of China for Excellent Young Scholars (41522502) and the China Special Fund for Meteorological Research in the Public Interest (GYHY201506013).

Appendix A

The nonlinear local Lyapunov vector and exponent spectrum

The evolution equation for the dynamical system is:

$$\dot{\boldsymbol{x}} = \frac{d\boldsymbol{x}}{dt} = \boldsymbol{F}(\boldsymbol{x}, t), \tag{8}$$

where $\boldsymbol{x}(t) = \left(x_1(t), x_2(t), \ldots, x_n(t)\right)^T$ represents the state vector of the dynamical system $\boldsymbol{F}$ at time t. Considering a small perturbation $\boldsymbol{\delta}(t) \in \mathbb{R}^{\mathrm{d}}$:

$$\frac{\boldsymbol{d}(\boldsymbol{x}(t) + \boldsymbol{y}(t))}{dt} = \boldsymbol{F}(\boldsymbol{x} + \boldsymbol{\delta}, t). \tag{9}$$

The governing equation for $\boldsymbol{\delta}(t)$ is:

$$\boldsymbol{\delta}(\dot{t}) = \boldsymbol{F}(\boldsymbol{x}(t) + \boldsymbol{\delta}(t)) - \boldsymbol{F}(\boldsymbol{x}(t)). \tag{10}$$

Without the tangent linear approximation, the solution of the perturbation $\boldsymbol{\delta}(t)$ is given by:

$$\boldsymbol{\delta}(\dot{t}_2) = \boldsymbol{DF}(\boldsymbol{x}(t_1))\boldsymbol{\delta}(t_1) + \boldsymbol{G}(\boldsymbol{x}(t_1), \boldsymbol{\delta}(t_1)), \tag{11}$$

where $\boldsymbol{DF}(\boldsymbol{x}(t))\boldsymbol{\delta}(t)$ are the tangent linear terms, and $\boldsymbol{G}(\boldsymbol{x}(t), \boldsymbol{y}(t))$ are the nonlinear terms of the perturbation $\boldsymbol{\delta}$(t). This is a high order nonlinear differential equations so cannot be solved analytically. However, we can obtain the

solution by numerically integrating the equation along the reference solution from t = t_1 to t_2:

$$\boldsymbol{\delta}(t_2) = \boldsymbol{\eta}(\boldsymbol{x}(t_1), \boldsymbol{\delta}(t_1), t_2 - t_1)\boldsymbol{\delta}(t_1), \tag{12}$$

where $\boldsymbol{\eta}(\boldsymbol{x}(t_1), \boldsymbol{\delta}(t_1), t_2 - t_1)$ is defined as the nonlinear propagator (Ding and Li 2007), which propagates the initial perturbation forward to $t = t_2$. This nonlinear propagator depends on the initial perturbation $\boldsymbol{\delta}(t_1)$. In order to obtain the growth rates of the perturbations corresponding to a certain size and a certain initial position, we need to find the growth directions in phase space and numerically compute the dynamical system with the perturbations. As mentioned above, the error vectors at a certain size tend to fall along the fastest growing directions as perturbations evolve over time in the dynamical system. In order to obtain the growth directions, we first breed the initial random perturbation $\boldsymbol{\delta}'(t_0)$, and after sufficient time $\boldsymbol{\tau}$, $\boldsymbol{\delta}'(t_0 + \tau)$ will capture the fastest growing direction. We take the direction of $\boldsymbol{\delta}'(t_0 + \tau)$ as the initial error $\boldsymbol{\delta}_1(t_0)$. The first (largest) nonlinear local Lyapunov exponent (NLLE) along the growing direction $\boldsymbol{\delta}_1(t_0)$ can be approximately defined as:

$$\lambda_1\left(\boldsymbol{x}(t_0), \boldsymbol{\delta}_1(t_0), \tau\right) = \frac{1}{\tau} \ln \frac{\boldsymbol{\delta}_1(t_0 + \tau)}{\boldsymbol{\delta}_1(t_0)}, \tag{13}$$

where $\lambda_1\left(\boldsymbol{x}(t_0), \boldsymbol{\delta}_1(t_0), \tau\right)$ depends on the initial state in phase space $\boldsymbol{x}(t_0)$, the initial perturbation $\boldsymbol{\delta}_1(t_0)$ and evolution time $\boldsymbol{\tau}$. Time-dependent Lyapunov exponents are obtained under the tangent linear equations so they do not depend on the perturbation size in the numerical calculation. A relationship exists between the first NLLE and the time-dependent Lyapunov exponent $\mu_1(t)$. In the limit as $\boldsymbol{\delta}_1(t_1) \to 0$ the first NLLE corresponds to the time-dependent Lyapunov exponent $\mu_1(t)$. When $\boldsymbol{\delta}_1(t_1) \to 0$, $\tau \to \infty$, the first NLLE converges to the largest Lyapunov exponent $\boldsymbol{\mu}_1$. The first NLLE has been used extensively to research the predictability of weather and climate (Ding et al. 2010, 2011, 2016; Li and Ding 2011, 2013).

As stated above, the n largest Lyapunov exponents characterize the growth rate of an n-dimensional volume of small perturbations. Continuing this inherent characteristic of the Lyapunov exponents, the first n largest NLLEs should describe the growth rate of a set of orthogonal perturbations. We define $\boldsymbol{\delta}_1(t_0), \boldsymbol{\delta}_2(t_0), \ldots, \boldsymbol{\delta}_n(t_0)$ as the nonlinear local Lyapunov vectors (NLLVs), which are orthogonal and correspond to the directions of the NLLEs. Through the evolution of the nonlinear system, $\boldsymbol{\delta}_1(t_0), \boldsymbol{\delta}_2(t_0), \ldots, \boldsymbol{\delta}_n(t_0)$ evolve into the vectors $\boldsymbol{\delta}'_1(t_0 + \tau), \boldsymbol{\delta}'_2(t_0 + \tau), \ldots, \boldsymbol{\delta}'_n(t_0 + \tau)$ through the breeding process. The ith NLLE $\lambda_i(x(t_0), \delta(t_0), \tau)$ can be determined directly from the growth rate of vector $\delta_i(t_0)$ (Feng et al. 2016, 2014; Li and Wang 2008):

$$\lambda_i\left[x(t_0), \delta_i(t_0), \tau\right] = \frac{1}{\tau} \log \frac{\left\|\delta_i(t_0 + \tau)\right\|}{\left\|\delta_i(t_0)\right\|} \ (i = 1, 2, \ldots, m). \tag{14}$$

The NLLVs $\boldsymbol{\delta}_1(t_0), \boldsymbol{\delta}_2(t_0), \ldots, \boldsymbol{\delta}_m(t_0)$ can be derived through a periodic reorthogonalization by the GSR process and rescaled (Feng et al. 2014; Li and Wang 2008). This process (as shown in Fig. 1) is similar to the breeding method (Toth and Kalnay 1997) but with the addition of periodical orthogonalization. Therefore, we also call the process of solving for NLLVs a breeding process. The breeding process is composed of multiple breeding cycles. In the GSR procedure, the direction of the first NLLV is never affected, which corresponds to the first NLLE, and the next fastest growing NLLV is orthogonalized with the first few NLLVs.

Appendix B

The ensemble Kalman filter

We first integrate the ZC model to acquire the long-term model state as the true state that is denoted by $\boldsymbol{x}_{\text{true}}$. The simulated observations $\boldsymbol{y}$ are generated from the true state using

$$\boldsymbol{y} = \boldsymbol{H}\boldsymbol{x}_{\text{true}} + \boldsymbol{\varepsilon}, \tag{15}$$

where $\boldsymbol{H}$ is a function mapping from the model space to the observation space, and $\boldsymbol{\varepsilon}$ represents independent realizations of the noise with a Gaussian distribution. The ensemble of forecast states is adopted as a set of background states. The ensemble is then defined as

$$\boldsymbol{X}_{\text{f}} = (\boldsymbol{x}_{\text{f},1}, \boldsymbol{x}_{\text{f},2}, ..., \boldsymbol{x}_{\text{f,N}}). \tag{16}$$

$\bar{\boldsymbol{x}}_f$ represents the mean of the ensemble. Then, an ensemble perturbation matrix can be written as:

$$\boldsymbol{X}'_{\text{f}} = (\boldsymbol{x}_{\text{f},1} - \bar{\boldsymbol{x}}_{\text{f}}, \boldsymbol{x}_{\text{f},2} - \bar{\boldsymbol{x}}_{\text{f}}, \ldots, \boldsymbol{x}_{\text{f,N}} - \bar{\boldsymbol{x}}_{\text{f}}). \tag{17}$$

The covariance matrix of the ensemble $\boldsymbol{X}_{\text{f}}$ is:

$$\boldsymbol{P}_f = \frac{1}{N-1}\boldsymbol{X}'_f\boldsymbol{X}'^T_f. \tag{18}$$

The background forecast ensemble will be updated by the observations. The observations are assimilated to generate a new analysis of the state:

$$\boldsymbol{x}_{a,i} = \boldsymbol{x}_{f,i} + \boldsymbol{K}\left(\boldsymbol{y} - \boldsymbol{H}\boldsymbol{x}_{f,i}\right), \quad i = 1, 2, \ldots, N, \tag{19}$$

where $\boldsymbol{K}$ is the Kalman gain. It is calculated by:

$$\boldsymbol{K} = \boldsymbol{P}_{\text{f}}\boldsymbol{H}^{\text{T}}\left(\boldsymbol{H}\boldsymbol{P}_{\text{f}}\boldsymbol{H}^{\text{T}} + \boldsymbol{R}\right)^{-1}, \tag{20}$$

where $\boldsymbol{R}$ is the observational error covariance matrix. $\boldsymbol{K}$ is actually a weight measuring the ratio of the forecast and observational error covariance.

The ensemble has 200 members, which is much smaller than the model dimension. Filtering divergence occurs in the EnKF assimilation process because of undersampling.

To overcome this problem, a 5% variance inflation factor is applied to $\boldsymbol{X}'_{\mathrm{f}}$ in this ZC model. Moreover, the localization technique is applied to the matrix $\boldsymbol{P}_{\mathrm{f}}$ to prevent spurious correlations at large distances. This is realized by the fifth-order function of Gaspari and Cohn (1999) with the distance of zero correlation equal to four grid lengths (almost 1000 km). The assimilation cycles are repeated for 1 month in each case to generate the analysis states. The mean $\bar{\boldsymbol{x}}_a$ of the analysis ensemble $\boldsymbol{x}_{a,i}$ ($i = 1, 2..., N$) is regarded as the initial state when performing the prediction.

References

Baehr J, Piontek R (2014) Ensemble initialization of the oceanic component of a coupled model through bred vectors at seasonal-to-interannual timescales. Geosci Model Dev 7:453–461. doi:10.5194/gmd-7-453-2014

Barnston AG, Tippett MK, van den Dool HM, Unger DA (2015) Toward an improved multimodel ENSO prediction. J Appl Meteorol Climatol 54:1579–1595

Bishop CH, Toth Z (1999) Ensemble transformation and adaptive observations. J Atmos Sci 56:1748–1765. doi:10.1175/1520-0469(1999)056<1748:ETAAO>2.0.CO;2

Blumenthal MB (1991) Predictability of a coupled ocean–atmosphere model. J Clim 4:766–784. doi:10.1175/1520-0442(1991)004<0766:POACOM>2.0.CO;2

Bowler NE (2006) Comparison of error breeding, singular vectors, random perturbations and ensemble Kalman filter perturbation strategies on a simple model. Tellus Ser A Dyn Meteorol Oceanogr 58:538–548. doi:10.1111/j.1600-0870.2006.00197.x

Buizza R, Palmer TN (1998) Impact of ensemble size on ensemble prediction. Mon Weather Rev 126:2503–2518

Buizza R, Houtekamer PL, Pellerin G, Toth Z, Zhu Y, Wei M (2005) A comparison of the ECMWF, MSC, and NCEP global ensemble prediction systems. Mon Weather Rev 133:1076–1097. doi:10.1175/MWR2905.1

Cai M, Kalnay E, Toth Z (2003) Bred vectors of the Zebiak–Cane model and their potential application to ENSO predictions. J Clim 16:40–56

Chen DK, Cane MA, Zebiak SE (1999) The impact of NSCAT winds on predicting the 1997/1998 El Nino: a case study with the Lamont–Doherty Earth Observatory model. J Geophys Res 104:11321–11327. doi:10.1029/98jc02543

Chen D, Cane MA, Kaplan A, Zebiak SE, Huang D (2004) Predictability of El Niño over the past 148 years. Nature 428:733–736. doi:10.1038/nature02439

Chen B, Li J, Ding R (2006) Nonlinear local Lyapunov exponent and atmospheric predictability research. Sci China Ser D Earth Sci 49:1111–1120. doi:10.1007/s11430-006-1111-0

Cheng Y, Tang Y, Jackson P, Chen D, Zhou X, Deng Z (2010a) Further analysis of singular vector and ENSO predictability in the Lamont model—part II: singular value and predictability. Clim Dyn 35:827–840. doi:10.1007/s00382-009-0728-z

Cheng Y, Tang Y, Zhou X, Jackson P, Chen D (2010b) Further analysis of singular vector and ENSO predictability in the Lamont model—part I: singular vector and the control factors. Clim Dyn 35:807–826. doi:10.1007/s00382-009-0595-7

Ding R, Li J (2007) Nonlinear finite-time Lyapunov exponent and predictability. Phys Lett Sect A Gen At Solid State Phys 364:396–400. doi:10.1016/j.physleta.2006.11.094

Ding R, Li J, Seo K-H (2010) Predictability of the Madden–Julian oscillation estimated using observational data. Mon Weather Rev 138:1004–1013. doi:10.1175/2009MWR3082.1

Ding R, Li J, Seo K-H (2011) Estimate of the predictability of boreal summer and winter intraseasonal oscillations from observations. Mon Weather Rev 139:2421–2438. doi:10.1175/2011MWR3571.1

Ding R, Li J, Zheng F, Feng J, Liu D (2016) Estimating the limit of decadal-scale climate predictability using observational data. Clim Dyn 46:1563–1580. doi:10.1007/s00382-015-2662-6

Duan WS, Mu M (2009) Conditional nonlinear optimal perturbation: applications to stability, sensitivity, and predictability. Sci China Ser D Earth Sci 52:883–906. doi:10.1007/s11430-009-0090-3

Duan W, Zhao P (2014) Revealing the most disturbing tendency error of Zebiak–Cane model associated with El Niño predictions by nonlinear forcing singular vector approach. Clim Dyn 44:2351–2367. doi:10.1007/s00382-014-2369-0

Duan W, Liu X, Zhu K, Mu M (2009) Exploring the initial errors that cause a significant "spring predictability barrier" for El Niño events. J Geophys Res 114:1–12. doi:10.1029/2008jc004925

Duan W, Tian B, Xu H (2014) Simulations of two types of El Niño events by an optimal forcing vector approach. Clim Dyn 43:1677–1692. doi:10.1007/s00382-013-1993-4

Epstein ES (1969) A scoring system for probability forecasts of ranked categories. J Appl Meteorol 8:985–987

Evensen G (2003) The ensemble Kalman filter: theoretical formulation and practical implementation. Ocean Dyn 53:343–367. doi:10.1007/s10236-003-0036-9

Feng J, Ding R, Liu D, Li J (2014) The application of nonlinear local Lyapunov vectors to ensemble predictions in Lorenz systems. J Atmos Sci 71:3554–3567. doi:10.1175/JAS-D-13-0270.1

Feng J, Ding R, Li J, Liu D (2016) Comparison of nonlinear local Lyapunov vectors with bred vectors, random perturbations and ensemble transform Kalman filter strategies in a barotropic model. Adv Atmos Sci 33:1036–1046. doi:10.1007/s00376-016-6003-4

Gaspari G, Cohn SE (1999) Construction of correlation functions in two and three dimensions. Q J R Meteorol Soc 125:723–757

Ginelli F, Poggi P, Turchi A, Chaté H, Livi R, Politi A (2007) Characterizing dynamics with covariant Lyapunov vectors. Phys Rev Lett 99:130601

Hastenrath S (1995) Recent advances in tropical climate prediction. J Clim 8:1519–1532

Houtekamer PL, Derome J (1995) Methods for ensemble prediction. Mon Weather Rev 123:2181–2196. doi:10.1175/1520-0493(1995)123<2181:MFEP>2.0.CO;2

Houtekamer PL, Zhang F (2016) Review of the ensemble Kalman filter for atmospheric data assimilation. Mon Weather Rev. doi:10.1175/MWR-D-15-0440.1 **(MWR-D-15-0440.0441)**

Ju J, Slingo J (1995) The Asian summer monsoon and ENSO. Q J R Meteorol Soc 121:1133–1168

Kalnay E (2003) Atmospheric modeling, data assimilation, and predictability. Cambridge University Press

Kirtman BP, Min D (2009) Multimodel ensemble ENSO prediction with CCSM and CFS. Mon Weather Rev 137:2908–2930. doi:10.1175/2009MWR2672.1

Legras B, Vautard R (1996) A guide to Liapunov vectors. In: Proceedings 1995 ECMWF seminar on predictability, pp 143–156

Leith CE (1974) Theoretical skill of Monte Carlo forecasts. Mon Weather Rev 102:409–418. doi:10.1175/1520-0493(1974)102<0409:TSOMCF>2.0.CO;2

Li J, Ding R (2011) Temporal–spatial distribution of atmospheric predictability limit by local dynamical analogs. Mon Weather Rev 139:3265–3283. doi:10.1175/MWR-D-10-05020.1

Li J, Ding R (2013) Temporal–spatial distribution of the predictability limit of monthly sea surface temperature in the global oceans. Int J Climatol 33:1936–1947. doi:10.1002/joc.3562

Li J, Wang S (2008) Some mathematical and numerical issues in geophysical fluid dynamics and climate dynamics. Commun Comput Phys 3:759–793

Lorenz EN (1965) A study of the predictability of a 28-variable atmospheric model. Tellus A 17:321–333. doi:10.3402/tellusa.v17i3.9076

May DA, Parmeter MM, Olszewski DS, McKenzie BD (1998) Operational processing of satellite sea surface temperature retrievals at the Naval Oceanographic Office. Bull Am Meteorol Soc 79:397–407

McPhaden MJ, Zebiak SE, Glantz MH (2006) ENSO as an integrating concept in earth science. Science 314:1740–1745. doi:10.1126/science.1132588

Meehl GA, Goddard L, Boer G, Burgman R, Branstator G, Cassou C, Corti S, Danabasoglu G, Doblas-Reyes F, Hawkins E, Karspeck A, Kimoto M, Kumar A, Matei D, Mignot J, Msadek R, Navarra A, Pohlmann H, Rienecker M, Rosati T, Schneider E, Smith D, Sutton R, Teng H, Van Oldenborgh GJ, Vecchi G, Yeager S (2014) Decadal climate prediction an update from the trenches. Bull Am Meteorol Soc 95:243–267. doi:10.1175/BAMS-D-12-00241.1

Molteni F, Buizza R, Palmer TN, Petroliagis T (1996) The ECMWF ensemble prediction system: methodology and validation. Q J R Meteorol Soc 122:73–119. doi:10.1002/qj.49712252905

Moore AM, Kleeman R (1998) Skill assessment for ENSO using ensemble prediction. Q J R Meteorol Soc 124:557–584. doi:10.1002/qj.49712454609

Mu M, Xu H, Duan W (2007) A kind of initial errors related to "spring predictability barrier" for El Niño events in Zebiak–Cane model. Geophys Res Lett 34:1–6. doi:10.1029/2006gl027412

Murphy AH (1973) A new vector partition of the probability score. J Appl Meteorol 12:595–600

Murphy J (1988) The impact of ensemble forecasts on predictability. Q J R Meteorol Soc 114:463–493

Palmer TN, Gelaro R, Barkmeijer J, Buizza R (1998) Singular vectors, metrics, and adaptive observations. J Atmos Sci 55:633–653. doi:10.1175/1520-0469(1998)055<0633:SVMAAO>2.0.CO;2

Patil D, Hunt BR, Kalnay E, Yorke JA, Ott E (2001) Local low dimensionality of atmospheric dynamics. Phys Rev Lett 86:5878

Peña M, Kalnay E (2004) Separating fast and slow modes in coupled chaotic systems. Nonlinear Process Geophys 11:319–327

Randall DA, Wood RA, Bony S, Colman R, Fichefet T, Fyfe J, Kattsov V, Pitman A, Shukla J, Srinivasan J (2007) Climate models and their evaluation. Climate change 2007: the physical science basis. Contribution of Working Group I to the Fourth Assessment Report of the IPCC (FAR). Cambridge University Press, pp 589–662

Reynolds RW (1988) A real-time global sea surface temperature analysis. J Clim 1:75–87

Saha S, Moorthi S, Wu X, Wang J, Nadiga S, Tripp P, Behringer D, Hou YT, Chuang HY, Iredell M, Ek M, Meng J, Yang R, Mendez MP, Van Den Dool H, Zhang Q, Wang W, Chen M, Becker E (2014) The NCEP climate forecast system version 2. J Clim 27:2185–2208. doi:10.1175/JCLI-D-12-00823.1

Shukla J, Anderson J, Baumhefner D, Brankovic C, Chang Y, Kalnay E, Marx L, Palmer T, Paolino D, Ploshay J, Schubert S, Straus D, Suarez M, Tribbia J (2000) Dynamical seasonal prediction. Bull Am Meteorol Soc 81:2593–2606. doi:10.1175/1520-0477(2000)081<2593:DSP>2.3.CO;2

Smith DM, Cusack S, Colman AW, Folland CK, Harris GR, Murphy JM (2007) Improved surface temperature prediction for the coming decade from a global climate model. Science 317:796–799

Szunyogh I, Kalnay E, Toth Z (1997) A comparison of Lyapunov and optimal vectors in a low-resolution GCM. Tellus Ser A Dyn Meteorol Oceanogr 49:200–227. doi:10.1034/j.1600-0870.1997.00004.x

Tang Y, Deng Z (2011) Bred vector and ENSO predictability in a hybrid coupled model during the period 1881–2000. J Clim 24:298–314. doi:10.1175/2010JCLI3491.1

Tang Y, Kleeman R, Moore AM (2005) Reliability of ENSO dynamical predictions. J Atmos Sci 62:1770–1791. doi:10.1175/JAS3445.1

Toth Z, Kalnay E (1993) Ensemble forecasting at NMC: the generation of perturbations. Bull Am Meteorol Soc 74:2317–2330. doi:10.1175/1520-0477(1993)074<2317:EFANTG>2.0.CO;2

Toth Z, Kalnay E (1997) Ensemble forecasting at NCEP and the breeding method. Mon Weather Rev 125:3297–3319. doi:10.1175/1520-0493(1997)125<3297:EFANAT>2.0.CO;2

Vialard J, Vitart F, Balmaseda MA, Stockdale TN, Anderson DLT (2005) An ensemble generation method for seasonal forecasting with an ocean–atmosphere coupled model. Mon Weather Rev 133:441–453. doi:10.1175/MWR-2863.1

Wang X, Bishop CH (2003) A comparison of breeding and ensemble transform Kalman filter ensemble forecast schemes. J Atmos Sci 60:1140–1158. doi:10.1175/1520-0469(2003)060<1140:ACOBAE>2.0.CO;2

Wei M, Toth Z (2003) A new measure of ensemble performance: Perturbation versus error correlation analysis (PECA). Mon Weather Rev 131:1549–1565. doi:10.1175//1520-0493(2003)131<1549:ANMOEP>2.0.CO;2

Wei M, Toth Z, Wobus R, Zhu Y, Bishop CH, Wang X (2006) Ensemble transform Kalman filter-based ensemble perturbations in an operational global prediction system at NCEP. Tellus Ser A Dyn Meteorol Oceanogr 58:28–44. doi:10.1111/j.1600-0870.2006.00159.x

Wilks DS (2011) Statistical methods in the atmospheric sciences. Academic press

Wittenberg AT, Rosati A, Lau N-C, Ploshay JJ (2006) GFDL's CM2 global coupled climate models. Part III: tropical Pacific climate and ENSO. J Clim 19:698–722

Wolf A, Swift JB, Swinney HL, Vastano JA (1985) Determining Lyapunov exponents from a time series. Phys D 16:285–317

Wu X (2016) Improving EnKF-based initialization for ENSO prediction using a hybrid adaptive method. J Clim 29:7365–7381

Yang SC, Cai M, Kalnay E, Reinecker M, Yuan G, Toth Z (2006) ENSO bred vectors in coupled ocean–atmosphere general circulation models. J Clim 19:1422–1436. doi:10.1175/JCLI3696.1

Yang S-C, Kalnay E, Cai M, Rienecker MM (2008) Bred vectors and tropical pacific forecast errors in the NASA coupled general circulation model. Mon Weather Rev 136:1305–1326. doi:10.1175/2007MWR2118.1

Yang SC, Keppenne C, Reinecker M, Kalnay E (2009) Application of coupled bred vectors to seasonal-to-interannual forecasting and ocean data assimilation. J Clim 22:2850–2870. doi:10.1175/2008JCLI2427.1

Yang SC, Rienecker M, Keppenne C (2010) The impact of ocean data assimilation on seasonal-to-interannual forecasts: a case study of the 2006 El Ni??o event. J Clim 23:4080–4095. doi:10.1175/2010JCLI3319.1

Zebiak SE, Cane MA (1987) A model El Nino–Southern oscillation. Mon Weather Rev 115:2262–2278. doi:10.1175/1520-0493(1987)115<2262:AMENO>2.0.CO;2

Zhang Z, Ren B, Zheng J (2017) Leading modes of tropical Pacific subsurface ocean temperature and associations with two types of El Nino. Sci Rep 7:42371. doi:10.1038/srep42371

Zheng F, Zhu J, Zhang RH, Zhou GQ (2006) Ensemble hindcasts of SST anomalies in the tropical Pacific using an intermediate coupled model. Geophys Res Lett 33. doi:10.1029/2006GL026994

Zheng F, Zhu J, Wang H, Zhang RH (2009) Ensemble hindcasts of ENSO events over the past 120 years using a large number of ensembles. Adv Atmos Sci 26:359–372. doi:10.1007/s00376-009-0359-7

Zhu YJ, Toth Z (2008) 2.2 Ensemble based probabilistic forecast verification